Published in final edited form as:
Remote Sens Environ. 2018 October ; 217: 72–85. doi:10.1016/j.rse.2018.08.005.

The Collection 6 MODIS burned area mapping algorithm and product

Louis Giglio[a,*], **Luigi Boschetti**[b], **David P. Roy**[c], **Michael L. Humber**[a], **Christopher O. Justice**[a]

[a]Department of Geographical Sciences, University of Maryland, College Park, MD, USA

[b]Department of Natural Resources and Society, University of Idaho, Moscow, ID, USA

[c]Geospatial Science Center of Excellence, South Dakota State University, Brookings, SD, USA

Abstract

The two Moderate Resolution Imaging Spectroradiometer (MODIS) instruments on-board NASA's Terra and Aqua satellites have provided nearly two decades of global fire data. Here, we describe refinements made to the 500-m global burned area mapping algorithm that were implemented in late 2016 as part of the MODIS Collection 6 (C6) land-product reprocessing. The updated algorithm improves upon the heritage Collection 5.1 (C5.1) MCD64A1 and MCD45A1 algorithms by offering significantly better detection of small burns, a modest reduction in burn-date temporal uncertainty, and a large reduction in the extent of unmapped areas. Comparison of the C6 and C5.1 MCD64A1 products for fifteen years (2002–2016) on a regional basis shows that the C6 product detects considerably more burned area globally (26%) and in almost every region considered. The sole exception was in Boreal North America, where the mean annual area burned was 6% lower for C6, primarily as a result of a large increase in the number of small lakes mapped (and subsequently masked) at high latitudes in the upstream C6 input data. With respect to temporal reporting accuracy, 44% of the C6 MCD64A1 burned grid cells were de-tected on the same day as an active fire, and 68% within 2 days, which represents a substantial reduction in temporal uncertainty compared to the C5.1 MCD64A1 and MCD45A1 products. In addition, an areal accuracy assessment of the C6 burned area product undertaken using high resolution burned area reference maps derived from 108 Landsat image pairs is reported.

Keywords

Fire; Biomass burning; Burned area; MODIS; MCD64A1

1. Introduction

The availability of remotely sensed terrestrial observations from NASA's Moderate Resolution Imaging Spectroradiometer (MODIS) instruments has yielded an extensive

[*]Corresponding author at: Department of Geographical Sciences, University of Maryland, 2181 LeFrak Hall, College Park, MD 20742, USA. lgiglio@umd.edu (L. Giglio), luigi@uidaho.edu (L. Boschetti), david.roy@sdstate.edu (D.P. Roy), mhumber@umd.edu (M.L. Humber), cjustice@umd.edu (C.O. Justice).

suite of global land, oceanic, and atmospheric data sets designed to meet the science and applications needs of the global change community (Justice et al., 1998). Within this suite are the MCD45A1 and MCD64A1 burned area products, which map the spatial extent and approximate date of biomass burning worldwide at a spatial resolution of 500 m. Both products have been used to conduct a broad range of research concerning biomass burning over the past decade (e.g., Andela et al., 2017; Archibald et al., 2009; Chen et al., 2016; Grégoire et al., 2013; Hantson et al., 2015; Lehmann et al., 2014; Oliveras et al., 2014; Petrenko et al., 2012; Randerson et al., 2012; Vadrevu et al., 2012; Yang et al., 2014). In addition, since 2006 the MCD64A1 product has been a major component of the Global Fire Emissions Database (Giglio et al., 2010, 2013; van der Werf et al., 2006, 2010, 2017), which has in turn been used in the investigation of a similarly broad set of research questions (e.g., Chen et al., 2013; DeFries et al., 2008; Larkin et al., 2014; Magi et al., 2012; Nevison et al., 2008; Schultz et al., 2008; Spessa et al., 2015; van der Werf et al., 2008, 2013).

Far from existing in isolation, NASA's MCD64A1 and MCD45A1 products are but two members of a larger ensemble of remotely-sensed global burned area data sets derived from what is, by contemporary standards, coarse spatial resolution (250 m–1 km) satellite imagery. Within this group also reside the 1-km L3JRC and 300-m Copernicus PROBA-V Burnt Area products (Tansey et al., 2008), and ESA's 1-km GLOBCARBON (Plummer et al., 2006), 300-m Fire_cci v4.1 (Chuvieco et al., 2016), and 250-m Fire_cci v5.0 products (Chuvieco et al., 2018).

Reprocessing is a fundamental requirement for producing consistent, science quality data sets suitable for long-term monitoring. The MODIS instrument data and products have been reprocessed into different Collections using updated calibration and geolocation information, and improved algorithms refined in response to routine product quality assessment and periodic validation activities (Justice et al., 2002b).

Here, we describe refinements made to the MCD64A1 burned area mapping algorithm and associated product for Collection 6, which is the third major reprocessing of the MODIS time series for which a burned area product has been generated. The Collection 6 MCD64A1 product, which supersedes both of its Collection 5.1 MCD45A1 and MCD64A1 predecessors, is intended to improve upon those earlier versions. We begin by briefly summarizing the status of the MODIS burned area products in Section 2. In Section 3, we describe the Collection 6 MCD64A1 algorithm, emphasizing those aspects that changed since Collection 5.1. In Section 4, we provide a brief global and regional intercomparison of the Collection 5.1 and Collection 6 MCD64A1 products. Finally, in Section 5, we present a temporal and areal accuracy assessment of the Collection 5.1 and Collection 6 MCD45A1 and MCD64A1 burned area products performed using MODIS active fire data and high-resolution Landsat burned area reference maps.

2. MCD45A1 and MCD64A1 product status

The MCD45A1 product was first produced and made publicly available in mid-2008 as part of the Collection 5 (C5) MODIS land product suite. The MCD45A1 mapping algorithm modelled on a tem-porally rolling basis the bidirectional effects in the daily MODIS time

series to identify persistent changes and in surface reflectance due to burning (Roy et al., 2005b, 2002). Initial validation results indicated that the product captured about 75% of the total area burned across southern Africa (Roy and Boschetti, 2009). Various algorithm changes intended to reduce certain types of omission and commission errors subsequently followed, with a reprocessed Collection 5.1 (C5.1) released in mid-2013.

The C5 MCD64A1 product (at the time not yet named as such) was first released in late 2009 in conjunction with the version 3 Global Fire Emissions Database (GFED) (Giglio et al., 2010). Minor adjustments were made over the next several years, directed primarily at reducing (albeit only slightly) an excessive loss of small agricultural burns in cropland, culminating in the release of the global C5.1 MCD64A1 product in late 2012. Unlike MCD45A1, the MCD64A1 mapping algo-rithm is a hybrid one that supplements daily surface reflectance imagery with daily active fire data. The algorithm is a major extension to an earlier hybrid approach used by (Roy et al., 1999) to map savanna burns in southern Africa with 1.1-km Advanced Very High Resolution Radiometer (AVHRR) imagery.

Assessment of the MCD45A1 and MCD64A1 products has been conducted under various regional validation efforts for Southern Africa, Siberia, central Asia, boreal Eurasia, Russian croplands, the Brazilian cerrado, Alaska, and the western conterminous United States through comparison with high-resolution satellite (typically Landsat) imagery (Giglio et al., 2009; Hall et al., 2016; Libonati et al., 2015; Loboda et al., 2011, 2012; Roy and Boschetti, 2009; Tsela et al., 2014; Zhu et al., 2017). At present, global assessment is limited to Padilla et al. (2014) and Padilla et al. (2015), who validated six global burned area data sets (including MCD45A1 and MCD64A1) for the 2008 calendar year using reference maps derived from Landsat-5 TM and SLC-off Landsat-7 ETM image pairs. The authors reported global commission and omission errors for both MODIS products of approximately 44% and 70%, respectively, with slightly lower error rates for MCD64A1. These figures should be viewed with caution as the rigorous temporal sampling strategies recommended for validation scene selection by Boschetti et al. (2016) and by Padilla et al. (2017) were not adopted by Padilla et al. (2014) during the selection of the Landsat reference imagery.

The broadly applicable findings of the above efforts may be sum-marized as follows: 1) both MODIS products often fail to map small (≲100 ha) burns, 2) the omission of small burns is significant in croplands (~10× underestimate), and 3) a much lower proportion of un-mapped areas exists in the MCD64A1 than the MCD45A1 product be-cause the latter is considerably more sensitive to cloud- and aerosol-contaminated observations and data gaps. Overall, both C5.1 burned area products tend to under-report burned area, in some regions quite substantially.

Based on these results, and given the cost of maintaining two separate operational MODIS production codes, the MODIS fire science team elected to retire the MCD45A1 product with C5.1 and implement Collection 6 (C6) refinements to the MCD64A1 algorithm. Those refinements are described in the next section.

3. Collection 6 MCD64A1 algorithm description

The C6 MCD64A1 burned-area detection algorithm uses as inputs the MODIS C6 Terra and Aqua 500-m atmospherically-corrected Level 2G daily surface reflectance products (Vermote and Justice, 2002), denoted MOD09GHK and MYD09GHK, respectively, and the C6 1-km Terra (MOD14A1) and Aqua (MYD14A1) Level 3 daily active fire products (Justice et al., 2002a), replicated to 500-m resolution, and the 500-m Level 3 MODIS annual land cover product, denoted MCD12Q1 (Friedl et al., 2010). The C6 MCD64A1 algorithm, like the previous C5.1 MCD64A1 algorithm, uses the most recently available C5.1 MCD12Q1 land cover product that was made for each year from 2001 to 2013, and substitutes the 2013 C5.1 MCD12Q1 product for 2014 onward. The MODIS Level 2G and Level 3 products are defined in the sinusoidal projection in fixed geolocated tiles approximately 1100 km × 1100 km in size (Wolfe et al., 1998).

The algorithm proceeds through multiple stages (Fig. 1), processing in each instance a single MODIS tile. The general approach is to produce composite imagery summarizing persistent changes in the time series of a burn-sensitive vegetation index, and then use spatial and temporal active-fire information to guide the statistical characterization of burn-related and non-burn-related change. This information is used to estimate probabilistic thresholds suitable for classifying individual 500-m grid cells as either *burned or unburned*.

Although the algorithm is capable of mapping burning over arbitrary time periods, for C6 the mapping period is constrained to a single calendar month. One month of daily observations before and after the mapping period are required to accommodate the moving windows employed in the change-detection process. Consequently, three consecutive months of observations are required to map one calendar month of burning. The approximate day of burning in each month is reported for each 500-m grid cell.

3.1. Time series extraction

Valid daily 0.65 μm (band 1), 1.24 μm (band 5), and 2.13 μm (band7) reflectance values are extracted from the Terra and Aqua Level 2G surface reflectance products using the four criteria previously described in Giglio et al. (2009): valid daily observations are 1) cloud-free (based on the MO/YD09 internal cloud mask), 2) fire-free (based on the MOD14/MYD14 active fire product), 3) acquired over land, and 4) have physically valid reflectance, i.e., > 0 and ≤ 1, for bands 1, 5, and 7. When multiple daytime observations are available for a 500-m grid cell on the same day, a single daily reflectance value is selected by choosing the cloud-free observation sensed at the smallest view zenith angle. This selection helps to reduce bidirectional reflectance effects that, across the MODIS swath, can be greater than reflectance changes due only to burning (Roy et al., 2002), and because observations sensed at smaller view zenith angles have finer spatial resolution (Wolfe et al., 1998). Bidirectional effects that remain are reduced through a temporal averaging process, described in Section 3.2, thus mitigating the need for BRDF-corrected surface reflectance data as an algorithm input.

Adopting the notation of Giglio et al. (2009), we denote the daily reflectance values selected for bands 1, 5, and 7 as $\rho_{1,i}$, $\rho_{5,i}$, and $\rho_{7,i}$, respectively, where the index i numbers the

individual days for which valid observations are available ($i = 1,2,3,\ldots,N$). A record of the ordinal day of year for each observation, denoted as t_i, is also recorded.

For Collection 6, it was necessary to impose an additional test that overrides a cloud commission error in the MOD09 internal cloud mask that occurs in certain low-reflectance situations and is often related to wet soil, due to, for example, snow melt or after heavy rainfall. Regardless of the underlying cause, no visual evidence of cloud cover is apparent for these problem cases. To this end, observations flagged as cloudy that also have a red reflectance $\rho_{1,i} \leq 0.12$ are treated as clear.

The daily reflectance values are used to compute the daily burnsensitive vegetation index $VI_i = (\rho_{5,i} - \rho_{7,i}) / (\rho_{5,i} + \rho_{7,i})$ for each grid cell. As noted by Roy and Landmann (2005) and Giglio et al. (2009), this spectral index, which shows a significant decrease after a burn, provides good burned-unburned discrimination.

3.2. Composite change summary

In this phase, the algorithm produces change- and fire-related composite imagery for subsequent classification. With the exception of the shortened temporal windows described below, this aspect of the algorithm remains unchanged from Collection 5, and consequently is described only briefly here. The reader is referred to Giglio et al. (2009) for a more detailed description.

The algorithm first examines the daily VI time series at each grid cell by considering observations within two non-overlapping adjacent sliding temporal windows, each containing $W = 8$ successive daily MODIS observations. These windows are referred to as the *candidate pre-burn and candidate post-burn* windows, respectively. Here a smaller window was adopted for Collection 6 (previously, $W = 10$ days) to re-duce the number of unclassified grid cells due to persistent cloud cover, and to reduce the temporal uncertainty in the burn date estimated for each burned grid cell.

Following the convention of Giglio et al. (2009), we use the index k to reference the temporal position of the adjacent windows as they are moved through the $N - 2W + 1$ distinct positions within the time series of the grid cell at location (x,y). At each temporal position, the 10% trimmed mean and trimmed standard deviation of the VI ob-servations within the candidate pre- and post-burn windows are calculated, denoted as $VI_{pre}(x,y,k)$, $\sigma_{pre}(x,y,k)$, $VI_{post}(x,y,k)$, and $\sigma_{post}(x,y,k)$, respectively. The trimmed summary statistics are derived in the conventional manner. If the number of observations is not an integer multiple of 10 (the 10% trim proportion) then appropriate weights are applied to the individual observations prior to the summary statistic calculation. For example, to calculate the 10% trimmed mean of 8 observations, the largest and smallest values are weighted by a factor of 0.2 and the remaining observations are weighted by a factor of 1.

Grid cells having too few valid observations to fill the candidate pre-and post-burn windows are immediately labeled as *unclassified* and subsequently ignored. Otherwise, a measure of temporal separability, S, is evaluated for all k:

$$S(x, y, k) = \frac{\Delta\ \mathrm{VI}(x, y, k)}{\left[\sigma_{\mathrm{pre}}(x, y, k) + \sigma_{\mathrm{post}}(x, y, k)\right]/2}, \quad (1)$$

where $\Delta\mathrm{VI}(x,y,k) = \mathrm{VI}_{\mathrm{pre}}(x,y,k) - \mathrm{VI}_{\mathrm{post}}(x,y,k)$. The properties of this measure are discussed by Giglio et al. (2009). In brief, abrupt decreases in the VI time series, such as those expected as the result of a fire, will yield large positive values of S.

The maximum value of S within the time series (i.e., the maximum separability) is identified for each grid cell, and the value of k at which this maximum occurs is designated k^*. Recorded for this event is the day associated with maximum VI separability, $t^*(x,y)$, the uncertainty in the date of maximum separability, $\Delta t^*(x,y)$, the corresponding absolute change in VI, $\Delta\mathrm{VI}(x,y,k^*)$, and the associated candidate post-burn VI, $\mathrm{VI}_{\mathrm{post}}(x,y,k^*)$. Following the convention of Giglio et al. (2009), we adopt for legibility the more concise notation $\Delta\mathrm{VI}^*(x,y) \equiv \Delta\mathrm{VI}(x,y,k^*)$, $\mathrm{VI}_{\mathrm{post}}{}^*(x,y) \equiv \mathrm{VI}_{\mathrm{post}}(x,y,k^*)$, etc., hereafter.

Included also in the change summary is the interquartile range (IQR) of the dates spanned by the maximum-separability pre- and post-burn windows, denoted $\mathrm{IQR}^*_{\mathrm{pre}}(x,y)$ and $\mathrm{IQR}^*_{\mathrm{post}}(x,y)$, respectively, which, as described in Giglio et al. (2009), are used to robustly determine if the time period spanned by either window is excessively long. In this situation, specifically if either $\mathrm{IQR}^*_{\mathrm{pre}}(x,y)$ or $\mathrm{IQR}^*_{\mathrm{post}}(x,y)$ exceeds 30 days, the grid cell is tentatively classified as unburned and ignored during subsequent processing until the final classification phase (Section 3.10).

Last among the composites is a cumulative mask, $t_{\mathrm{f}}(x,y)$, identifying in each grid cell the date on which an active fire was detected (if any) during the three-month time period being processed. If multiple fires were detected during the compositing period, the date nearest to $t^*(x,y)$ is chosen.

A complete list of all composited spatial variables is provided in Table 1.

3.3. Temporal texture

As previously noted by Giglio et al. (2009), the day of maximum change (t^*) usually shows much higher spatial coherence in burned patches than unburned patches. To exploit this additional textural information, the algorithm computes the local standard deviation of t^* within a small circular kernel, defined on the reference spheroid by a circle of 500 m radius from the centroid of each 500-m grid cell. Because the sinusoidal projection is neither conformal nor equidistant, when projected onto the MODIS grid this kernel assumes the form of an ellipse having a location-dependent size and orientation; the cells whose centroid falls inside the kernel constitute the local neighborhood from which the standard deviation is computed (Fig. 2). In most locations, the kernel includes five cells (a center and four neighbors), although only three and four cells can occur away from the Equator and the prime meridian.

To prevent the loss of fine, 1-grid-cell sections of burned patches, the texture map is filtered with an edge-restoring ranked order filter (Astola and Kuosmanen, 1997) that selects

the 25th percentile within the kernel (here, calculation of the 25th percentile may require inter-polation when the number of grid cells contained within the kernel is not four). As in the original algorithm description, the resulting filtered temporal texture is denoted σ_t^* (x, y).

3.4. Selection of training samples

The cumulative active-fire composite described above is used to help identify representative burned and unburned training samples that are used during the subsequent supervised classification phase of the algorithm. As we have previously cautioned, the identification process requires careful consideration of both resampling error as well as the special characteristics of active fire data (Giglio et al., 2009). The composited active-fire map consequently undergoes a process of spatial and temporal cleaning coupled with region growing to prevent excessive cross-contamination of the respective training samples.

3.4.1. A-priori unburned grid cells—Selection of training samples begins by identifying grid cells that are highly unlikely to have burned during the mapping period. As in the Collection 5 algorithm, the grid cell at location (x,y) is identified as unburned *a priori* if $S^*(x,y) < 2$ (i.e., spectral separability is too low) or σ_t^* (x, y) > 8 days (i.e., spatial coherence is too low).

3.4.2. Burned training grid cells—A"clean" subset of those grid cells flagged as fire in the cumulative active fire mask is used to create an initial training mask of burned grid cells. The cleaning process consists of morphological erosion followed by a series of spatial and temporal threshold tests. The subset of grid cells that remain comprise the *initial burned training mask*. Full details are found in Giglio et al. (2009).

To reduce the impact of under-sampling of spatial fire extent by MODIS active fire observations, the initial burned training mask is expanded through a process of region growing which considers ΔVI^*, VI_{post}^*, and σ_t^*, constrained by a maximum growth distance of 10 km. For C6, this procedure remains exactly as described in Giglio et al. (2009), with the exception that the region growing is not performed for those grid cells within the initial burned training mask that are classified as cropland in the MCD12Q1 land cover product. This stipulation helps reduce the likelihood of commission errors within broad swaths of cropland during the harvest season.

The end result of the region growing procedure is a *burned training mask*, which is used to extract burned training samples during the next phase of the algorithm.

3.4.3. Unburned training grid cells—In producing a complementary mask of unburned training pixels, we exploit information from the *a priori* unburned grid cells (Section 3.4.1) as well as the burned training mask (Section 3.4.2). As in Giglio et al. (2009), the grid cell at location (x,y) is flagged as an unburned training grid cell if either of the following conditions is satisfied: 1) the grid cell is an *a priori* unburned grid cell, or 2) the grid cell contains valid data, is not included among the burned training observations, and has $d_B(x,y) > R_d$, where the parameter R_d is the "dilation radius" (Giglio et al., 2009) and

the function $d_B(x,y)$ denotes the distance from location (x,y) to the nearest grid cell within the burned training mask.

For Collection 5, the parameter R_d was nominally fixed at 5 km but modified for tiles encompassing Africa and during the Terra-only period prior to mid-2002. For Collection 6, R_d is now coupled to the parameter σ_p used during the assignment of prior probabilities (Section 3.7) such that $R_d = 2.5\sigma_p$ (ultimately this will mean that R_d can assume a value of either 5 km or 12.5 km). The new coupling maintains consistency with this later algorithm phase, as both phases share the assumption that distant grid cells (i.e., those distant from burned training cells) are less likely to have burned.

3.5. Extraction of conditional probability densities

In this step, which remains unchanged for C6, the burned and unburned training samples obtained above are used to derive the conditional burned (B) and unburned (U) probability density functions (PDFs) $P_l(\Delta VI^*|B)$ and $P_l(\Delta VI^*|U)$ for each land cover type l present in the MODIS tile being processed. To estimate these densities we use a Gaussian kernel density estimator, $P(u)$, with normalization factor C and standard deviation $\sigma_k = 0.02$, given by

$$P(u) = C \sum_i \exp\left(-\frac{[u - u_i]^2}{2\sigma_k^2}\right), \quad (2)$$

with the summation taken over each observation in the training sample.

3.6. Separability test

The ΔVI* burned and unburned conditional probability distributions for each land cover class are at this point tested to ensure they differ suffciently to permit burned and unburned grid cells to be discriminated. Previously, an overly strict criterion based on the Hellinger distance, a quantitative measure of the overlap between two probability distributions (Upton and Cook, 2002), was used. For Collection 6, we adopted more relaxed criteria that are less sensitive to noise that can appear in the tails of the ΔVI* distributions, particularly when the number of training samples is small. The Collection 6 tests are based upon the medians (50th percentiles) of the land-cover-specific burned and unburned conditional ΔVI* training samples, which we denote as $Q_l^{(50)}$ (ΔVI*|B) and $Q_l^{(50)}$ (ΔVI*|U), respectively.

The separability criteria are applied to the difference in medians, $\Delta Q_l = Q_l^{(50)}$ (ΔVI*|B) − $Q_l^{(50)}$ (ΔVI*|U), and the number of observations (grid cells) in the burned training sample within each land cover class ($N_{B,l}$): If $\Delta Q_l < -0.05$, or if $\Delta Q_l \leq 0$ and $N_{B,l} < 100$, then all grid cells belonging to land cover class l are immediately classified as *unburned*, and processing continues for the remaining land cover classes present in the MODIS tile. Note that while $\Delta Q_l > 0$ is expected for “normal” burns, the C6 algorithm permits slightly negative values ($\Delta Q_l \geq -0.05$) to enable a minimal mapping capability during particularly illbehaved instances of cropland burning. However, when the burned training sample is small ($N_{B,l} < 100$), this is not permitted since the burned conditional PDF is inherently less reliable.

As a point of clarification, the *unclassified* vs. *unburned* labels to which a grid cell may be summarily categorized – the former during production of the composite change summary (Section 3.2), and the latter as just described when the separability criteria are not met – reflect the quite different circumstances encountered by the algorithm when these classes are summarily assigned. In the former case, no spectral information whatsoever can be extracted from the input data for the grid cell, and the *unclassified* label reasonably represents this state of complete ignorance. In the latter situation, however, the algorithm has a usable time series of observations but recognizes that there exists no discernable spectral difference between the unburned and burned training samples. In this indeterminate situation, the algorithm conservatively chooses the more likely scenario, which in at least most parts of the world would be that, at the scale of a MODIS tile, the majority of the grid cells associated with a specific land cover class do not burn over the span of a calendar month. Users objecting to this designation may easily track such grid cells with a flag set in the quality assurance layer of the MCD64A1 product.

3.7. Prior probabilities

The algorithm at this point establishes spatially explicit prior burned probabilities $P_B(x,y)$ in preparation for the application of Bayes' rule. With minor modification, the approach replicates that used for the C5 algorithm. All grid cells labeled a priori as unburned training cells are assigned $P_B(x,y) = 0$, otherwise the burned prior probability for the grid cell is computed as a function of its proximity to the nearest burned training cell using the Gaussian weighting function

$$P_B(x,y) = (P_{max} - P_{min})\exp\left(-\frac{d_B(x,y)^2}{2\sigma_p^2}\right) + P_{min}, \quad (3)$$

where $P_{max} = 0.5$ and $d_B(x,y)$ is the distance from grid cell (x,y) to the nearest burned training grid cell. Eq. (3) limits the range of the prior probability such that $P_{min} \leq P_B(x,y) \leq P_{max}$, with the maximum being attained at the location of each burned training grid cell. For the C5 algorithm, σ_p was fixed at 5 km and P_{min} was either 0.05 (Africa) or 0.02 (elsewhere). For the C6 algorithm, P_{min} is fixed at 0.01 while the former value of $\sigma_p = 5$ km is now retained only for African tiles but reduced to $\sigma_p = 2$ km elsewhere. Given Eq. (3), the prior unburned probability is derived as $P_U(x,y) = 1 - P_B(x,y)$.

As previously noted by Giglio et al. (2009), the prior probability in Eq. (3) provides a way to quantify our initial degree of belief that a specific grid cell was burned based on a subset of the remotely-sensed data available to the algorithm, and is based on the reasonable expectation that burns are more likely to occur in the proximity of other burns. At distances far from "known" (i.e., training) burned cells, the prior probability asymptotically approaches the minimum likelihood P_{min}. The comparatively low value specified for this parameter (0.01) reflects the fact, in general, any small, randomly selected patch of the land surface is highly unlikely to have burned during the past several months.

3.8. Posterior burned probability

As with the C5 algorithm, the posterior probability of the grid cell at location (*x,y*) and within land cover class *l* having burned during the compositing period, given the observed change in VI, is estimated using Bayes' rule:

$$P(\mathrm{B}|\ \Delta\ \mathrm{VI}^*(x,y)) = \frac{P_l(\ \Delta\ \mathrm{VI}^*|\mathrm{B})P_{\mathrm{B}}(x,y)}{P_l(\ \Delta\ \mathrm{VI}^*|\mathrm{B})P_{\mathrm{B}}(x,y) + P_l(\ \Delta\ \mathrm{VI}^*|\mathrm{U})P_{\mathrm{U}}(x,y)}. \quad (4)$$

We note that within our Bayesian framework the phrase "posterior probability of a grid cell having burned" used here represents our *revised degree of belief* that the grid cell actually burned; strictly speaking, the phrase "probability of having burned" is meaningless, as the mapping algorithm operates long after the event in question did or did not occur.

3.9. Initial classification

In this penultimate step, the algorithm produces a tentative classification of *burned or unburned* for each valid 500-m grid cell within the MODIS tile, excluding those cells summarily designated as *unburned* by the separability test (Section 3.6).

As with Collection 5, two relative thresholds are computed for each land cover class and employed during this step: $Q_l^{(98)}$ ($\mathrm{VI}^*_{\mathrm{post}}|\mathrm{B}$), the 98th percentile of the $\mathrm{VI}_{\mathrm{post}}$* burned training sample, and $Q_l^{(98)}$ (σ_t*|B), the 98th percentile of the σ_t* burned training sample. Grid cells satisfying the following four conditions, which are with one exception unchanged from Collection 5, are tentatively classified as *burned*:

1. the grid cell was not identified as an *a priori* unburned grid cell during the selection of training observations (Section 3.4.1);
2. the posterior probability $P_l(\mathrm{B}|\Delta\mathrm{VI}^*(x,y)) \geq 0.5$;
3. $\mathrm{VI}^*_{\mathrm{post}}(x,y) \leq Q_l^{(98)}(\mathrm{VI}^*_{\mathrm{post}}|\mathrm{B})$;
4. $\sigma_t^*(x,y) \leq Q_l^{(98)}(\sigma_l^*|B)$.

The sole change for Collection 6 occurs in condition (2), where the ΔVI* posterior probability threshold was reduced from 0.6 to 0.5 to reduce the frequency of omission errors. Grid cells that fail to satisfy one or more of the above conditions are tentatively classified as *unburned*.

3.10. Final classification

In this final step, additional contextual information is used to update as needed the label assigned to each grid cell during the previous step (Section 3.9). As with the C5 algorithm, the basis for this relabeling is a constrained majority filter, but with a modification intended to help capture small burns that were previously removed indiscriminately.

Input data Algorithm tuned for C6 MODIS surface reflectance and active fire products. Time series extraction (3.1) Adopted cloud minimum red-reflectance threshold to override MOD09 cloud mask. Change summary (3.2) Temporal window duration W reduced from

10 to 8days. Training samples (3.4) Region growing no longer performed in cropland. New parameter coupling: Rd=2.5σp. Separability test (3.6) Hellinger distance criterion eliminated; ΔVI* percentile criterion relaxed. Prior probabilities (3.7) Pmin reduced to 0.01; σp default value reduced to 2km. Initial classification (3.9) Posterior probability threshold reduced from 0.6 to 0.5. Final classification (3.10) Majority filter employs projection-aware kernel and is modulated using information derived from training data.

The C6 approach considers the number of tentatively burned grid cells (n_B) and tentatively unburned grid cells (n_U) within 500-m of the grid cell being processed, employing the projection-adjusted spatial kernel described in Section 3.3. Also considered is n_{CB}, the number of tentatively burned grid cells counted in n_B that are *temporally* consistent with the central grid cell being processed ($0 \le n_{CB} \le n_B$). Grid cells at adjacent locations (x,y) and (x',y') are considered to be temporally consistent if $|t^*(x,y) - t^*(x',y')| \le 10$ days. This 10-day threshold was found to reasonably accommodate spread rates typical of even comparatively "slow" fires, in combination with a practical 1- or 2-day minimum burn-date uncertainty.

Unlike the C5 algorithm, the C6 algorithm considers prior information about the likelihood that a burned grid cell will have burned neighbors. This prior knowledge is used to modulate the aggressiveness of the *burned-to-unburned* relabeling process. The specific information employed is the local cumulative conditional probability that a burned grid cell has n_B or fewer burned neighbors, $F(n_B|B)$, where

$$F(n_B|B) = P(N_B \le n_B|B) \tag{5}$$

$$= \sum_{N=0}^{n_B} P(N_B = N|B). \tag{6}$$

The conditional burned-neighbor probability (for random variable N_B, from which n_B is drawn) in Eq. (6) is independently estimated for each grid cell tentatively classified as *burned* during the initial classification phase by examining the surrounding neighborhood within 50-km of the grid cell. The true (i.e., non-estimated) probability is in fact circularly dependent on the final classification that this phase of the algorithm will ultimately produce. Consequently, the burned training mask produced earlier (Section 3.4.2) is used as a proxy burned area map to estimate $F(n_B|B)$. Representative examples of these cumulative probabilities for large savanna versus small cropland fires are shown in Fig. 3.

The Collection 6 final-classification relabeling scheme, which incorporates a new burned-neighbor cumulative probability filtering criterion, is as follows. A grid cell initially classified as *burned* is relabeled *unburned* if $n_U > n_B$ and $F(n_B|B) < 0.1$. Here, the latter criterion limits the elimination of small burned patches and isolated burned grid cells to those cases having an exceptionally low prior expectation of occurrence. Conversely, a grid cell initially classified as *unburned* is relabeled *burned* if $n_B > n_U$ and $n_{CB} \ge 1$.

Compared to the original algorithm, the C6 relabeling scheme typically yields a comparable population of grid cells relabeled from *unburned to burned*, but, on a global scale, a vastly reduced population relabeled from *burned to unburned*. We examine the impact of this new scheme in Section 4.

3.11. Summary of Collection 6 algorithm changes

As is clear from the preceding algorithm description, a number of significant changes were made to the original Giglio et al. (2009) ap-proach as part of the MODIS Collection 6 reprocessing effort. We provide a summary of those changes in Table 2.

We note that the C6 MCD64A1 algorithm includes a number of algorithm parameters, of which the majority are tuned empirically through a combination of physical insight, trial and error, and the authors' experience using MODIS and other satellite data, supplemented in some instances with sensitivity analyses. While it is not unreasonable to view this reliance on empirical tuning as a shortcoming, some important caveats should be kept in mind. We note first that many of the algorithm parameters (e.g., W) are highly constrained by physical quantities associated with fire behavior (e.g., the fire spread rate), the MODIS sensor (e.g., spatial resolution), and the orbital characteristics (e.g., repeat cycle) of the Terra and Aqua satellites on which the sensor resides. Second, a number of parameters are "innocuous" in the sense that the final output is relatively insensitive to the particular value chosen for the parameter. An example from this category is the smoothing parameter σ_k used in the Gaussian kernel density estimator. Third, fully one fourth of the algorithm parameters are fundamentally related to the suppression or management of noise (e.g., the 10% trim used during extraction of the time series). Employing automated methods to tune such parameters is often problematic since the numerical optimization is inherently inclined to overfit the very noise the parameters are meant to suppress. Finally, we note that for a global algorithm the number of empirical MCD64A1 parameters is not especially unusual among traditional burned area mapping algorithms developed for application over large spatial scales (e.g., Loboda et al., 2007; Alonso-Canas and Chuvieco, 2015). While recent machine-learning approaches (e.g., Ramo and Chuvieco, 2017) are in contrast comparatively parameter-free, this advantage is achieved at a cost of having the mapping algorithm expressed as a "black box" containing tens to hundreds or even thousands of individual weights or rules. Moreover, machine learning algorithms used for classification purposes require appropriate configuration prior to their application, and the optimal configuration is a subject of investigation (Wulder et al., 2018).

4. Comparison with Collection 5.1

To demonstrate the impact of the algorithm refinements described in Section 3 we performed a comparison of the C6 MCD64A1 and C5.1 MCD64A1 products for the years 2002–2016. A much more detailed comparison, including consideration of differences in seasonality, was conducted by Humber et al. (2018) as part of a larger, multi-product intercomparison. Note that the burned area component of the version 4 Global Fire Emissions Database (GFED4) from mid-2000 onward was derived from the C5.1 MCD64A1 product (Giglio et al., 2013),

hence the results presented here serve equivalently as a comparison between GFED4 and C6 MCD64A1.

To quantify gross regional differences, we computed the mean annual area burned globally and within the 14 sub-continental GFED regions loosely defined on the basis of fire behavior and their suitability for emission studies (Giglio et al., 2006). The smallest region, Central America (CEAM), encompasses an area of 2.7×10^6 km^2, and the largest, Central Asia (CEAS), encompasses an area of 18.1×10^6 km^2, corresponding to approximately 2% and 13% of the global land surface, excluding Antarctica, respectively (Boschetti and Roy, 2008). Overall, the C6 product maps significantly more burned area globally (26%) and in almost every region considered (Table 3). The sole exception was in Boreal North America (BONA), where the mean annual area burned was 6% lower for C6, primarily as a result of a large increase in the number of small lakes mapped (and subsequently masked) at high latitudes in the upstream input data (Fig. 4).

Of the 13 regions experiencing an increase in reported burned area for C6, the bulk of this newly mapped burned area appears as smaller patches typically 21 ha (i.e., one MODIS “500-m” grid cell) to ~100 ha in size (Fig. 5). A large proportion of these small burns in turn occur within cropland (Fig. 6), roughly doubling the reported cropland burned area in seven regions (TENA, CEAM, NHSA, SHSA, EURO, MIDE, BOAS, CEAS, and SEAS) for C6. Some portion of this additional area may be the result of commission errors associated with tilling and/ or harvesting, but it is also likely that the C6 MCD64A1 product still grossly under-reports the extent of cropland burning in many agricultural regions due to the assortment of complications that confound attempts to remotely sense this class of fires (Hall et al., 2016). The improved handling of small burned patches under Collection 6 similarly impacted the extent of burning mapped within forest throughout much of the tropics (CEAM, NHSA, SHSA, and SEAS), again approximately doubling the reported area burned (Fig. 6).

We note that the impact of any MCD12Q1 land cover product errors will be common to both the C5.1 and C6 MCD64A1 burned area products, as they both used the C5.1 MCD12Q1 product. The main intent in using the annual land cover classification data is to help ensure that phenology-related changes in the VI time series of one particular 500-m grid cell are not confused with burn-related changes in the VI time series of another. This is accomplished by “localizing” the conditional PDFs as well as the extent within the MODIS tile to which they apply. However, we note that the C6 algorithm change to no longer perform region growing for cropland burns is expected to be subject to errors in the MCD12Q1 cropland classification which globally is reported as 83.3% (producer’s accuracy) and 92.8% (user’s accuracy) (Friedl et al., 2010).

5. Accuracy assessment

5.1. Temporal uncertainty

We repeated the Boschetti et al. (2010b) temporal reporting accuracy and precision assessment for both the MCD45A1 and MCD64A1 burned area products (Fig. 7). The assessment examines the time difference between MODIS active fire and burned area

detections that occur within 90 days as a measure of temporal uncertainty. We found that, globally, 44% of the Collection 6 MCD64A1 burned grid cells were detected on the same day of an active fire, and 68% within 2 days, which represents a substantial reduction in temporal uncertainty compared to the Collection 5.1 MCD64A1 and (especially) MCD45A1 products.

5.2. Areal uncertainty

5.2.1. Preliminary global validation—A preliminary validation using a globally distributed independent reference data set (Fig. 8) consisting of 108 Landsat scenes visually interpreted into burned, unburned, and unmapped classes was undertaken. Landsat 5 Thematic Mapper (TM) images acquired from 2000 to 2010, and Landsat 7 Enhanced Mapper Plus (ETM+) images sensed from 2000 to 2003 before the ETM+ scan line corrector failure (Markham et al., 2004), were used. The scenes are distributed to cover a range of representative global burning conditions, but are not selected via probability sampling. The sampling provides a Stage 2 validation, i.e., the product accuracy is assessed over a widely distributed set of locations and time periods that represent the full range of conditions under which the product is expected to perform (Morisette et al., 2006). The independent reference data were derived following the protocol developed by members of the GOFC/GOLD Southern African Fire Network (SAFNet) (Roy et al., 2005a) and subsequently adopted by the Committee on Earth Observations (CEOS) Land Product Validation Working Group for use by the international community (Boschetti et al., 2010a). The CEOS validation protocol requires that global coarse re-solution burned area products (250 m–1 km spatial resolution) be validated using independent reference data derived from two or more Landsat-class images, allowing for comparison between the reference data and the burned areas detected by the global product in the period between acquisitions, with the exception of ecosystems (such as boreal forest) where burned areas are unambiguously visible in satellite data for more than an entire fire season. According to the protocol, the in-dependent reference data must be derived with minimum error, either by visual interpretation (Roy et al., 2005a; Roy and Boschetti, 2009; Giglio et al., 2009) or by application of a semi-automatic algorithm followed by visual checking and manual refinement (Boschetti et al., 2006; Padilla et al., 2014). All unobserved areas (e.g. due to clouds or shadows), or areas having spectral characteristics that could not be unambiguously interpreted, were masked and removed from further analysis.

The validation procedure is summarized as follows. The three MODIS burned area products (MCD64A1 C6, MCD64A1 C5.1, and MCD45A1 C5.1) were temporally composited to encompass the interval between the two Landsat acquisition dates. In the case of 24 boreal forest reference scenes in Siberia derived from the interpretation of single-date images (Loboda et al., 2007), the MODIS products were temporally composited from the first day of the year up to the Landsat acquisition date. The temporally composited MODIS products were subsequently reprojected into the UTM projection of each reference scene, with nearest neighbor resampling to the Landsat pixel size, to allow for direct pixel-by-pixel comparison between the classified and reference data.

The local scale accuracy was characterized by the confusion matrix, which reports the area agreement and disagreement between the classification and the reference data. Six commonly used pixel-level accu-racy metrics were derived from the confusion matrix: the overall ac-curacy (OA), the burned area omission error ratio ("omission error", OE), the commission error ratio ("commission error", CE), the producer's accuracy (PA), the user's accuracy (UA), and the relative bias (B_{rel}). Formulas for all metrics can be found in Padilla et al. (2015). Table 4 reports the error matrices and the accuracy metrics computed for the C6 and C5.1 MCD64A1 and the C5.1 MCD45A1 products, aggregated over the entire independent reference data set. The error matrices are reported in terms of area (km^2) as well as percentages. It should be noted that the difference in unmapped area of the three products leads to a different total mapped area in each matrix. The C6 MCD64A1 product had a slightly lower omission error than the C5.1 version (0.37 vs. 0.40) and a slightly higher commission error (0.24 vs 0.22); the C5.1 MCD45A1 product had a significantly higher omission error (0.45) than the other two products, and a similar commission error (0.23). All three products had similarly high overall accuracy (0.97), mostly reflecting the prevalence of the unburned class. The C6 MCD64A1 product also detects the highest total area burned among the three products (C6 MCD64A1: 100,327 km^2; C5.1 MCD64A1: 91,825 km^2; C5.1 MCD45A1: 83,332 km^2).

The slightly higher producer's accuracy (+2% absolute difference) and correspondingly lower omission error of the C6 MCD64A1 product might seem inconsistent with the 26% global increase in mean global burned area (compared to C5.1) we reported in Section 4. However, much of this increase is a consequence of the C6 algorithm now operating over a significantly expanded range of sub-optimal conditions that were reported as unmapped in the C5.1 product (Fig. 5). These C6 algorithm characteristics work in tandem to capture significantly more burned area than would be expected on the basis of our validation results alone.

A certain degree of error of omission and commission is due solely to the presence of mixed pixels (Boschetti et al., 2004), and the error matrix does not distinguish between these unavoidable errors, and er-rors due to misclassification. For this reason, the error matrix and the derived accuracy metrics were complemented by a regional scale accuracy assessment based on regression metrics. The proportion of 5 km coarse resolution grid cells detected as burned by the MODIS products is compared to the proportion of area detected by the reference data; the slope and offset of the regression line are an indication of the ac-curacy of the burned area detection, whereas the coeffcient of determination (r^2) is an indication of the precision. Fig. 9 reports the scatter plots obtained by combining all the cells from the 108 reference scenes. The analysis shows that the C6 MCD64A1 product has slightly higher accuracy and precision than the C5.1 MCD64A1 (slope: 0.88 vs. 0.85; r^2: 0.818 vs. 0.808), and significantly higher than the C5.1 MCD45A1 (slope: 0.76; r^2: 0.744).

5.2.2. Multitemporal accuracy assessment over small fires—One of the most significant changes in the Collection 6 algorithm is the preservation of small burned patches and isolated pixels. In order to assess the accuracy of detection on extremely small and fragmented fires, a time series of Landsat 8 Operational Land Imager (OLI) 30-m images was acquired over WRS path/row 200/051, located in Mali in the same area previously

studied by Laris (2005). In this region, the burned areas are spatially fragmented and small relative to the 500-m MODIS pixel dimension. Ten consecutive Landsat images, acquired from 28 September 2013 to 8 April 2014, were interpreted pair-wise, generating reference burned area maps covering the 2013–2014 fire season (Fig. 10). Fig. 11 reports the scatter plots of the proportion of area burned as detected by the Collection 6 MCD64A1 product and by the reference data, and the linear regression metrics computed following the same procedure described in Section 5.2.1. As a reference, each scatter plot reports also the regression line computed using the Collection 5.1 MCD64A1 and MCD45A1 products. With the exception of the first time interval at the beginning of the season (Fig. 11, upper left plot) when a few fires are entirely omitted, the slope of the re-gression line varies from a minimum of 0.083 to a maximum of 1.738, and the coeffcient of determination r^2 from 0.554 to 0.777.

6. Conclusions

We have described improvements made to the MCD64A1 burned area mapping algorithm as part of the MODIS Collection 6 land-product reprocessing. The updated algorithm improves upon the Collection 5.1 MCD64A1 and Collection 5.1 MCD45A1 mapping algorithms by offering significantly better detection of small burns, a modest reduction in burn-date temporal uncertainty, and a large reduction in the extent of unmapped areas. Our 2002–2016 comparison of the product with these previous MODIS products showed that, overall, the C6 product detects considerably more burned area globally (26%) and in almost every region considered. The sole exception was in Boreal North America, where the mean annual area burned was 6% lower for C6, primarily as a result of a large increase in the number of small lakes mapped (and subsequently masked) at high latitudes in the upstream input data.

We performed a temporal and areal accuracy assessment of the C5.1 and C6 products using MODIS active fire data and high resolution burned area reference maps derived from Landsat imagery. With respect to temporal reporting accuracy, 44% of the C6 MCD64A1 burned grid cells were detected on the same day of an active fire, and 68% within 2 days, which represents a substantial reduction in temporal uncertainty compared to the C5.1 MCD64A1 and MCD45A1 products. The areal accuracy assessment consisted of a preliminary CEOS Stage 2 validation using a reference dataset of 108 Landsat scenes. At the pixel level, the Collection 6 MCD64A1 product had a commission error of 0.24 and an omission error of 0.37; the linear regression computed using 5 km grid cells yielded a slope of 0.88, with coeffcient of determination $r^2 = 0.82$. The accuracy metrics of the Collection 5.1 MCD64A1 product were almost identical, whereas the MCD45A1 product had a higher omission error (0.45) and a lower linear regression slope (0.74). Because the reference dataset was not extracted via probability sampling, these figures cannot be extrapolated to the whole temporal and spatial domain of the product, and should be used only as an indication of relative importance. A global validation of the Collection 6 MCD64A1 burned area product to CEOS Stage 3, i.e., using a statistically robust and globally representative accuracy assessment that employs reference imagery selected via probability sampling, is planned. In closing, we note that the Collection 6 MCD64A1 algorithm and product is also the baseline for the forthcoming science-quality Suomi National Polar-orbiting Partnership

(S-NPP) Visible Infrared Imaging Radiometer Suite (VIIRS) VNP64A1 burned area product to be produced by NASA.

Acknowledgments

This work was supported by NASA grants NNX11AG42G and NNX14AI68G. We thank three anonymous reviewers and Editor-in-Chief E. Chuvieco for helpful comments and technical suggestions.

References

Alonso-Canas I, Chuvieco E, 2015. Global burned area mapping from ENVISAT-MERIS and MODIS active fire data. Remote Sens. Environ 163, 140–152.

Andela N, Morton DC, Giglio L, Chen Y, van der Werf GR, Kasibhatla PS, DeFries RS, Collatz GJ, Hantson S, Kloster S, Bachelet D, Forrest M, Lasslop G, Li F, Mangeon S, Melton JR, Yue C, Randerson JT, 2017. A human-driven decline in global burned area. Science 356, 1356–1362. [PubMed: 28663495]

Archibald S, Roy DP, Wilgen BWV, Scholes RJ, 2009. What limits fire? An ex-amination of drivers of burnt area in sub-equatorial Africa. Glob. Chang. Biol 15, 613–630.

Astola J, Kuosmanen P, 1997. Fundamentals of Nonlinear Digital Filtering CRC Press, Boca Raton.

Boschetti L, Brivio PA, Eva HD, Gallego J, Baraldi A, Grégoire J-M, 2006. A sampling method for the retrospective validation of global burned area products. IEEE Trans. Geosci. Remote Sens 44 (7), 1765–1773.

Boschetti L, Flasse S, Brivio PA, 2004. Analysis of the conflict between omission and commission in low spatial resolution thematic products: the Pareto Boundary. Remote Sens. Environ 91, 280–292.

Boschetti L, Roy DP, 2008. Defining a fire year for reporting and analysis of global interannual fire variability. J. Geophys. Res 113, G03020.

Boschetti L, Roy DP, Justice CO, 2010a. International global burned area satellite product validation protocol part i — production and standardization of validation reference data. Tech. rep. CEOS Working Group on Calibration and Validation https://lpvs.gsfc.nasa.gov/PDF/BurnedAreaValidationProtocol.pdf.

Boschetti L, Roy DP, Justice CO, Giglio L, 2010b. Global assessment of the temporal reporting accuracy and precision of the MODIS burned area product. Int. J. Wildland Fire 19, 705–709.

Boschetti L, Stehman SV, Roy DP, 2016. A stratified random sampling design in space and time for regional to global scale burned area product validation. Remote Sens. Environ 186, 465–478. [PubMed: 30416212]

Chen Y, Morton DC, Andela N, Giglio L, Randerson JT, 2016. How much global burned area can be forecast on seasonal time scales using sea surface temperatures? Environ. Res. Lett 11, 045001.

Chen Y, Morton DC, Jin Y, Collatz GJ, Kasibhatla PS, van der Werf GR, DeFries RS, Randerson JT, 2013. Long-term trends and interannual variability of forest, savanna and agricultural fires in South America. Carbon Manage 4 (6), 617–638.

Chuvieco E, Lizundia-Loiola J, Pettinari ML, Ramo R, Padilla M, Tansey K, Mouillot F, Laurent P, Storm T, Heil A, Plummer S, 2018. Generation and analysis of a new global burned area product based on modis 250 m reflectance bands and thermal anomalies. Earth Syst. Sci. Data Discuss https://www.earth-syst-sci-data-discuss.net/essd-2018-46/ In review.

Chuvieco E, Yue C, Heil A, Mouillot F, Alonso-Canas I, Padilla M, Pereira JM, Oom D, Tansey K, 2016. A new global burned area product for climate assessment of fire impacts. Glob. Ecol. Biogeogr 25, 619–629.

DeFries RS, Morton DC, van der Werf GR, Giglio L, Collatz GJ, Randerson JT, Houghton RA, Kasibhatla PK, Shimabukuro Y, 2008. Fire-related carbon emissions from land use transitions in southern Amazonia. Geophys. Res. Lett 35, L22705.

Friedl MA, Sulla-Menashe D, Tan B, Schneider A, Ramankutty N, Sibley A, Huang X, 2010. MODIS Collection 5 global land cover: algorithm refinements and char-acterization of new datasets. Remote Sens. Environ 114, 168–182.

Giglio L, Loboda T, Roy DP, Quayle B, Justice CO, 2009. An active-fire based burned area mapping algorithm for the MODIS sensor. Remote Sens. Environ 113, 408–420.

Giglio L, Randerson JT, van der Werf GR, 2013. Analysis of daily, monthly, and annual burned area using the fourth-generation global fire emissions database (GFED4). J. Geophys. Res. Biogeosci 118, 1–12.

Giglio L, Randerson JT, van der Werf GR, Kasibhatla PS, Collatz GJ, Morton DC, Defries RS, 2010. Assessing variability and long-term trends in burned area by merging multiple satellite fire products. Biogeosciences 7, 1171–1186.

Giglio L, van der Werf GR, Randerson JT, Collatz GJ, Kasibhatla PS, 2006. Global estimation of burned area using MODIS active fire observations. Atmos. Chem. Phys 6, 957–974.

Grégoire J-M, Eva HD, Belward AS, Palumbo I, Simonetti D, Brink A, 2013. Effect of land-cover change on Africa's burnt area. Int. J. Wildland Fire 22, 107–120.

Hall JV, Loboda TV, Giglio L, McCarty G, 2016. A MODIS-based burned area assessment for Russian croplands: mapping requirements and challenges. Remote Sens. Environ 184, 506–521.

Hantson S, Pueyo S, Chuvieco E, 2015. Global fire size distribution is driven by human impact and climate. Glob. Ecol. Biogeogr 24 (1), 77–86.

Humber ML, Boschetti L, Giglio L, Justice CO, 2018. Spatial and temporal inter-comparison of four global burned area products. Int. J. Digital Earth 1–25.

Justice CO, Giglio L, Korontzi S, Owens J, Morisette JT, Roy D, Descloitres J, Alleaume S, Petitcolin F, Kaufman Y, 2002a. The MODIS fire products. Remote Sens. Environ 83, 244–262.

Justice CO, Townshend JRG, Vermote EF, Masuoka E, Wolfe RE, Saleous N, Roy DP, Morisette J, 2002b. An overview of MODIS land data processing and product status. Remote Sens. Environ 83, 3–15.

Justice CO, Vermote E, Townshend JRG, Defries R, Roy DP, Hall DK, Salomonson VV, Privette JL, Riggs G, Strahler A, Lucht W, Myneni RB, Knyazikhin Y, Running SW, Nemani RR, Wan Z, Huete AR, van Leeuwen W, Wolfe RE, Giglio L, Muller J-P, Lewis P, Barnsley MJ, 1998. The Moderate Resolution Imaging Spectroradiometer (MODIS): land remote sensing for global change research. IEEE Trans. Geosci. Remote Sens 36 (4), 1228–1249.

Laris PS, 2005. Spatiotemporal problems with detecting and mapping mosaic fire regimes with coarse-resolution satellite data in savanna environments. Remote Sens. Environ 99, 412–424.

Larkin NK, Reffuse SM, Strand TM, 2014. Wildland fire emissions, carbon, and climate: U.S. emissions inventories. For. Ecol. Manag 317, 61–69.

Lehmann CER, Anderson TM, Sankaran M, Higgins SI, Archibald S, Hoffmann WA, Hanan NP, Williams RJ, Fensham RJ, Felfili J, Hutley LB, Ratnam J, Jose JS, Montes R, Franklin D, Russell-Smith J, Ryan CM, Durigan G, Hiernaux P, Haidar R, Bowman DMJS, Bond WJ, 2014. Savanna vegetation-fire-climate relationships differ among continents. Science 343, 548–552. [PubMed: 24482480]

Libonati R, DaCamara CC, Setzer AW, Morelli F, Melchiori AE, 2015. An algorithm for burned area detection in the Brazilian cerrado using 4μm MODIS imagery. Remote Sens 7, 15782–15803.

Loboda T, O'Neal KJ, Csiszar I, 2007. Regionally adaptable dNBR-based algorithm for burned area mapping from MODIS data. Remote Sens. Environ 109, 429–442.

Loboda TV, Giglio L, Boschetti L, Justice CO, 2012. Regional fire monitoring and characterization using global NASA MODIS fire products in dry lands of Central Asia. Front. Earth Sci 6 (2), 196–205.

Loboda TV, Hoy EE, Giglio L, Kasischke ES, 2011. Mapping burned area in Alaska using MODIS data: a data limitations-driven modification to the regional burned area algorithm. Int. J. Wildland Fire 20, 487–496.

Magi BI, Rabin S, Shevliakova E, Pacala S, 2012. Separating agricultural and non-agricultural fire seasonality at regional scales. Biogeosciences 9, 3003–3012.

Markham BL, Storey JC, Williams DL, Irons JR, 2004. Landsat sensor performance: history and current status. IEEE Trans. Geosci. Remote Sens 42 (12), 2691–2694.

Morisette JT, Baret F, Liang S, 2006. Special issue on global land product validation. IEEE Trans. Geosci. Remote Sens 44, 1695–1697.

Nevison CD, Mahowald NM, Doney SC, Lima ID, van der Werf GR, Randerson JT, Baker DF, Kasibhatla P, McKinley GA, 2008. Contribution of ocean, fossil fuel, land biosphere, and biomass burning carbon fluxes to seasonal and interannual variability in atmospheric CO_2. J. Geophys. Res. Biogeosci 113, G01010.

Oliveras I, Anderson LO, Malhi Y, 2014. Application of remote sensing to understanding fire regimes and biomass burning emissions of the tropical Andes. Glob. Biogeochem. Cycles 28, 480–496.

Padilla M, Olofsson P, Stehman SV, Tansey K, Chuvieco E, 2017. Stratification and sample allocation for reference burned area data. Remote Sens. Environ 0, 0.

Padilla M, Stehman SV, Chuvieco E, 2014. Validation of the 2008 MODIS-MCD45 global burned area product using stratified random sampling. Remote Sens. Environ 144, 187–196.

Padilla M, Stehman SV, Ramo R, Corti D, Hantson S, Oliva P, Alonso-Canas I, Bradley AV, Tansey K, Mota B, Pereira JM, Chuvieco E, 2015. Comparing the accuracies of remote sensing global burned area products using stratified random sampling and estimation. Remote Sens. Environ 160, 114–121.

Petrenko M, Kahn R, Chin M, Soja A, Kucsera T, Harshvardhan, 2012. The use of satellite-measured aerosol optical depth to constrain biomass burning emissions source strength in the global model GOCART. J. Geophys. Res. Atmos 117, D18212.

Plummer S, Arino O, Simon M, Steffen W, 2006. Establishing an Earth observation product service for the terrestrial carbon community: the GLOBCARBON initiative. Mitig. Adapt. Strateg. Glob. Chang 11 (1) 97–11.

Ramo R, Chuvieco E, 2017. Developing a random forest algorithm for MODIS global burned area classification. Remote Sens 9, 1193.

Randerson JT, Chen Y, van der Werf GR, Rogers BM, Morton DC, 2012. Small fire contributions to global burned area and biomass burning emissions. J. Geophys. Res 117, G04012.

Roy DP, Boschetti L, 2009. Southern Africa validation of the MODIS, L3JRC, and GlobCarbon burned-area products. IEEE Trans. Geosci. Remote Sens 47 (4), 1032–1044.

Roy DP, Frost P, Justice CO, Landmann T, Roux JL, Gumbo K, Makungwa S, Dunham K, Toit RD, Mhwandagara K, Zacarias A, Tacheba B, Dube O, Pereira J, Mushove P, Morisette J, Vannan SS, Davies D, 2005a. The Southern Africa Fire Network (SAFNet) regional burned area product validation protocol. Int. J. Remote Sens 26, 4265–4292.

Roy DP, Giglio L, Kendall JD, Justice CO, 1999. Multi-temporal active-fire based burn scar detection algorithm. Int. J. Remote Sens 20, 1031–1038.

Roy DP, Jin Y, Lewis PE, Justice CO, 2005b. Prototyping a global algorithm for systematic fire-affected area mapping using MODIS time series data. Remote Sens. Environ 97, 137–162.

Roy DP, Landmann T, 2005. Characterizing the surface heterogeneity of fire effects using multi-temporal reflective wavelength data. Int. J. Remote Sens 26, 4197–4218.

Roy DP, Lewis PE, Justice CO, 2002. Burned area mapping using multi-temporal moderate spatial resolution data — a bidirectional reflectance model-based expectation approach. Remote Sens. Environ 83, 263–286.

Schultz MG, Heil A, Hoelzemann JJ, Spessa A, Thonicke K, Goldammer J, Held AC, Pereira JM, 2008. Global emissions from wildland fires from 1960 to 2000. Glob. Biogeochem. Cycles 22, GB2002.

Spessa AC, Field RD, Pappenberger F, Langner A, Englhart S, Weber U, Stockdale T, Siegert F, Kaiser JW, Moore J, 2015. Seasonal forecasting of fire over Kalimantan, Indonesia. Nat. Hazards Earth Syst. Sci 15, 429–442.

Tansey K, Grégoire J-M, Defourny P, Leigh R, Pekel J-F, van Bogaert E, Bartholomé E, 2008. A new, global, multi-annual (2000–2007) burnt area product at 1 km resolution. Geophys. Res. Lett 35, L011401.

Tsela P, Wessels K, Botai J, Archibald S, Swanepoel D, Steenkamp K, Frost P, 2014. Validation of the two standard MODIS satellite burned-area products and an empirically-derived merged product in South Africa. Remote Sens 6, 1275–1293.

Upton G, Cook I, 2002. A Dictionary of Statistics Oxford University Press, Oxford.

Vadrevu KP, Ellicott E, Giglio L, Badarinath KVS, Vermote E, Justice CO, Lau WKM, 2012. Vegetation fires in the himalayan region — aerosol load, black carbon emissions and smoke plume heights. Atmos. Environ 47, 241–251.

van der Werf GR, Dempewolf J, Trigg SN, Randerson JT, Kasibhatla PS, Giglio L, Murdiyarso D, Peters W, Morton DC, Collatz GJ, Dolman AJ, DeFries RS, 2008. Climate regulation of fire emissions and deforestation in equatorial Asia. Proc. Natl. Acad. Sci 105 (51), 20350–20355. [PubMed: 19075224]

van der Werf GR, Peters W, van Leeuwen TT, Giglio L, 2013. What could have caused pre-industrial biomass burning emissions to exceed current rates? Clim. Past 9, 289–306.

van der Werf GR, Randerson JT, Giglio L, Collatz GJ, Kasibhatla PS, Arellano AF Jr., 2006. Interannual variability of global biomass burning emissions from 1997 to 2004. Atmos. Chem. Phys 6, 3423–3441.

van der Werf GR, Randerson JT, Giglio L, Collatz GJ, Mu M, Kasibhatla PS,Morton DC, DeFries RS, Jin Y, van Leeuwen TT, 2010. Global fire emissions and the contribution of deforestation, savanna, forest, agricultural, and peat fires (1997–2009). Atmos. Chem. Phys 10, 11707–11735. www.atmos-chem-phys.net/10/11707/2010/.

van der Werf GR, Randerson JT, Giglio L, van Leeuwen TT, Chen Y, Rogers BM, Mu M, van Marle MJE, Morton DC, Collatz GJ, Yokelson RJ, Kasibhatla PS, 2017. Global fire emissions estimates during 1997–2016. Earth Syst. Sci. Data 9, 697–720.

Vermote EF, Justice NZESCO, 2002. Operational atmospheric correction of the MODIS data in the visible to middle infrared: first results. Remote Sens. Environ 83, 97–111.

Wolfe RE, Roy DP, Vermote E, 1998. MODIS land data storage, gridding, and compositing methodology: level 2 grid. IEEE Trans. Geosci. Remote Sens 36, 1324–1338.

Wulder MA, Coops NC, Roy DP, White JC, Hermosilla T, 2018. Land cover 2.0. Int. J. Remote Sens 39 (12), 4254–4284.

Yang J, Tian H, Tao B, Ren W, Kush J, Liu Y, Wang Y, 2014. Spatial and temporal patterns of global burned area in response to anthropogenic and environmental factors: reconstructing global fire history for the 20th and early 21st centuries. J. Geophys. Res. Biogeosci 119, 249–263.

Zhu C, Kobayashi1 H, Kanaya Y, Saito M, 2017. Size-dependent validation of MODIS MCD64A1 burned area over six vegetation types in boreal Eurasia: large under-estimation in croplands. Sci. Report 7, 4181.

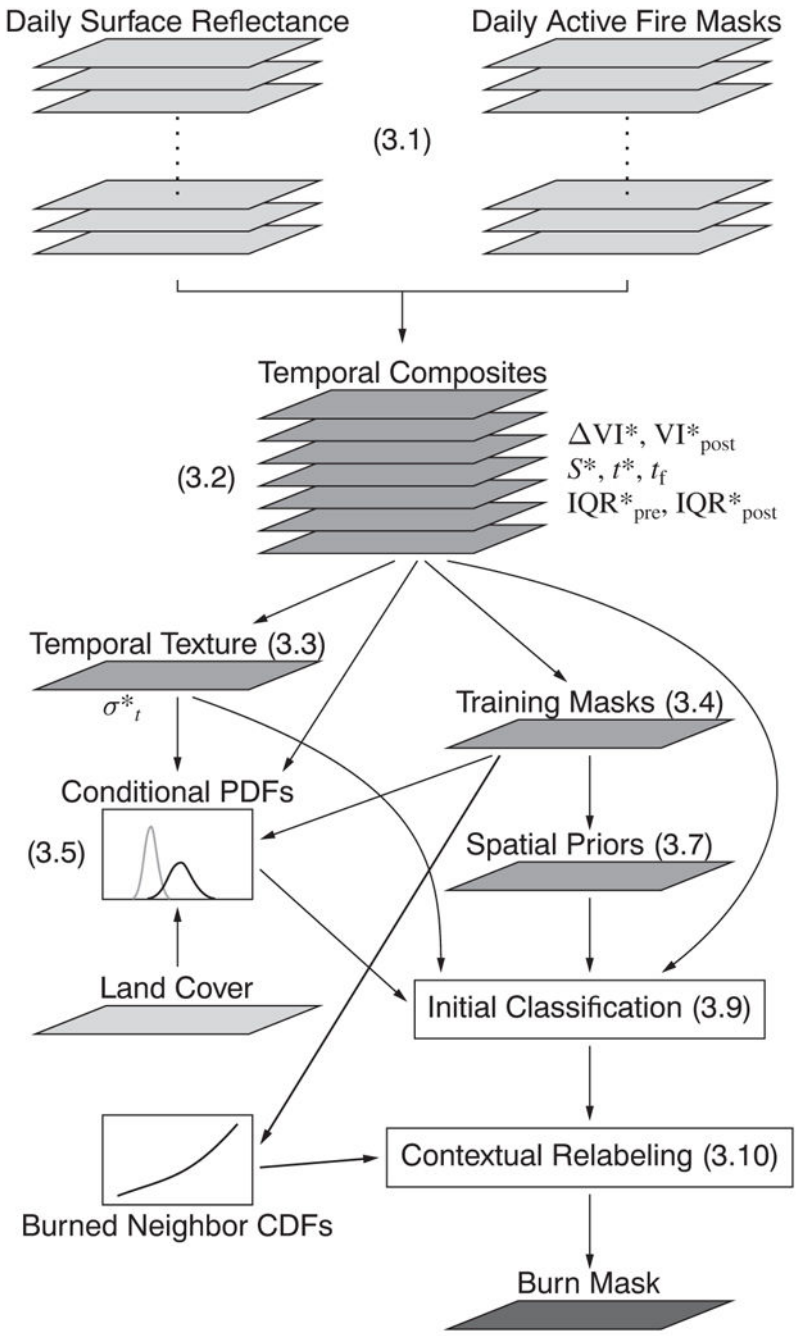

Fig. 1.

Flow chart of Collection 6 MCD64A1 burned area mapping algorithm, which is applied to individual tiles of the MODIS sinusoidal grid. Input data layers are shown in light grey, intermediate data layers computed internally as part of the algorithm are shown in medium grey, and final output map is shown in dark grey. Numbers in parentheses refer to section numbers in the main text.

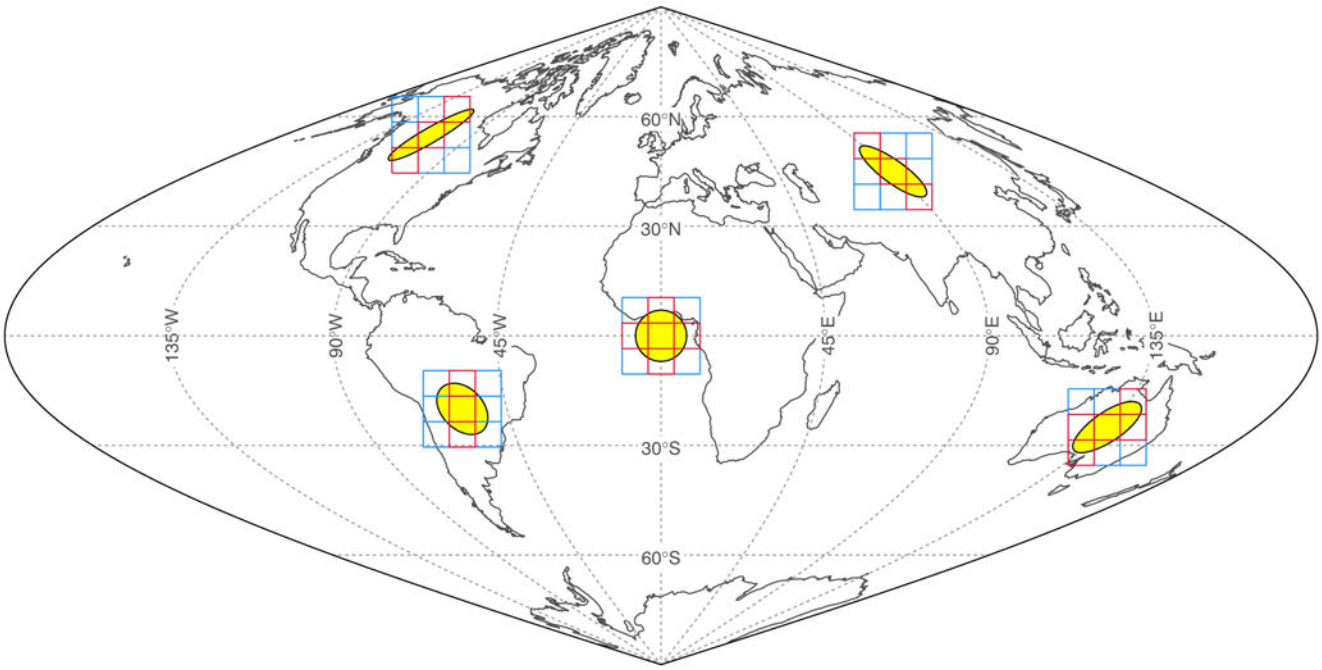

Fig. 2.

Representative examples at five locations of the equi-distant spatial kernels (shown in yellow) used by the Collection 6 MCD64A1 mapping algorithm. Within the MODIS sinusoidal projection plane, these kernels assume the form of ellipses having variable orientation and eccentricity. Superimposed on each kernel as red squares is the rasterized approximation for the specific case of a 500-m radius that operates on the gridded MODIS data. The examples shown here have been greatly magnified for clarity and are not drawn to scale. (For interpretation of the references to color in this figure legend, the reader is referred to the web version of this article.)

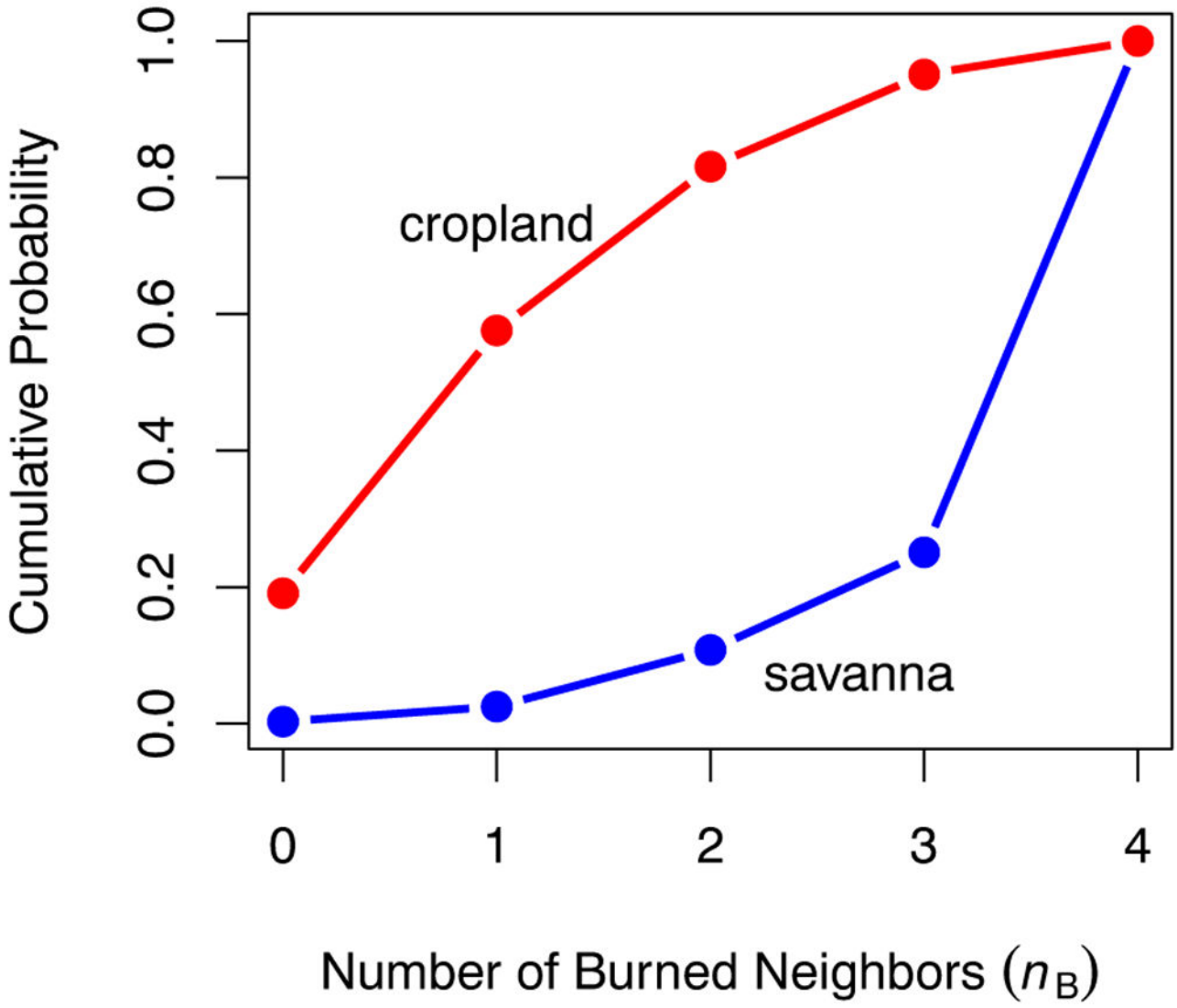

Fig. 3.

Example cumulative conditional burned-neighbor probability distribu-tions for savanna located in northern Australia (MODIS tile h31v10) versus cropland located in western Russia (tile h20v03). Within cropland, a full 20% of burned training cells have no burned neighbors, while in savanna only ~1% of burned training cells share this characteristic.

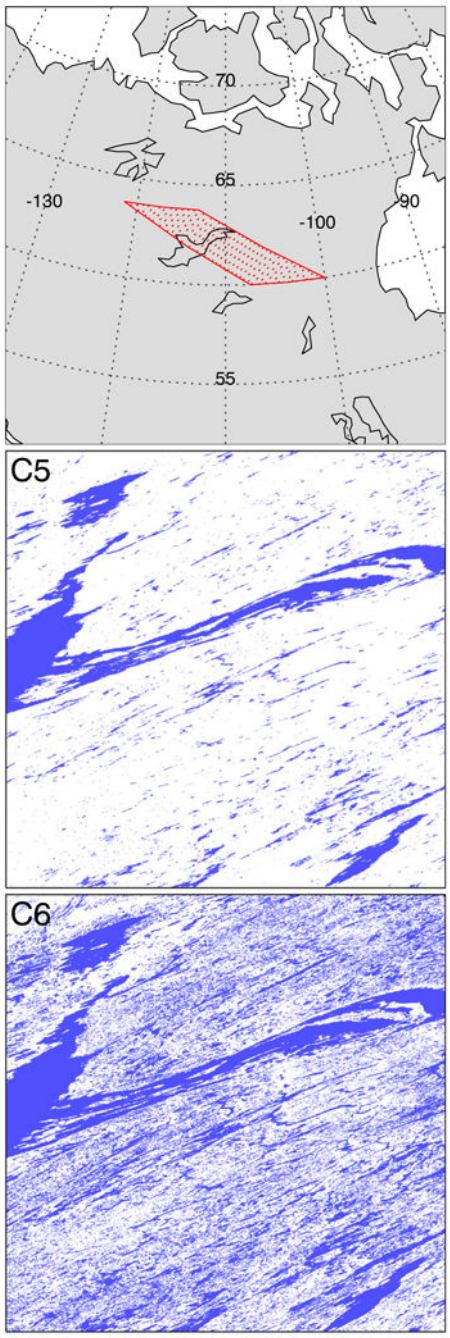

Fig. 4.

Example of MODIS Collection 5 and also Collection 5.1 (middle panel) and Collection 6 (bottom panel) MODIS land/water mask for a spatial subset of MODIS tile h12v02 (top panel, red outline) encompassing the western half of the Great Slave Lake in Northwest Territories, Canada. In this particular ex-ample, the increase in the number of small water bodies (shown in blue) mapped in Collection 6 is striking. The region shown in the lower two panels is approximately 830 km × 830 km in size. (For interpretation of the references to color in this figure legend, the reader is referred to the web version of this article.)

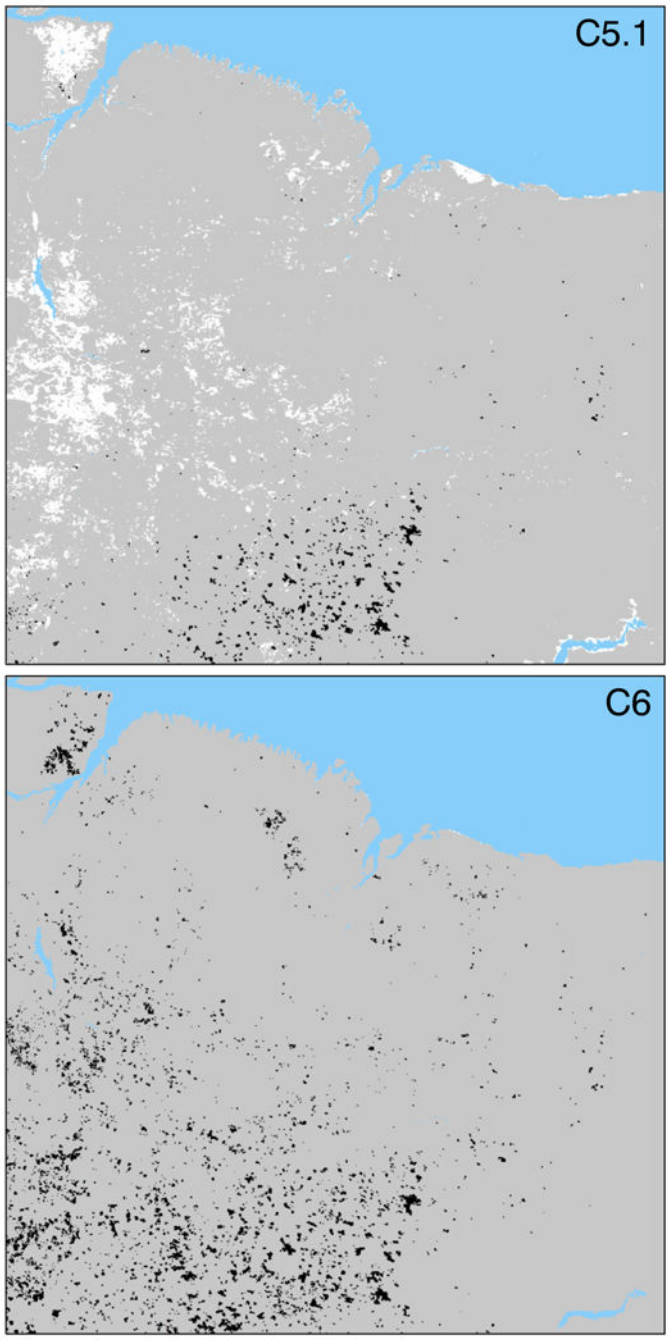

Fig. 5.

Collection 5.1 (top panel) and Collection 6 (bottom panel) MCD64A1 monthly burned area maps for September 2002 in MODIS tile h13v09, which overlaps eastern Brazil, illustrating the improved sensitivity to small burns and the reduction in unmapped grid cells. Unburned land grid cells are depicted in grey, unclassified areas in white, water in blue, and burned grid cells in black. In this formerly problematic case (due to persistent cloud cover), the 1.53 Mha of burned area mapped in the C6 product is four times greater than the 0.38 Mha mapped under C5.1. The tile is approximately 1100 km × 1100 km in size. (For

interpretation of the references to color in this figure legend, the reader is referred to the web version of this article.)

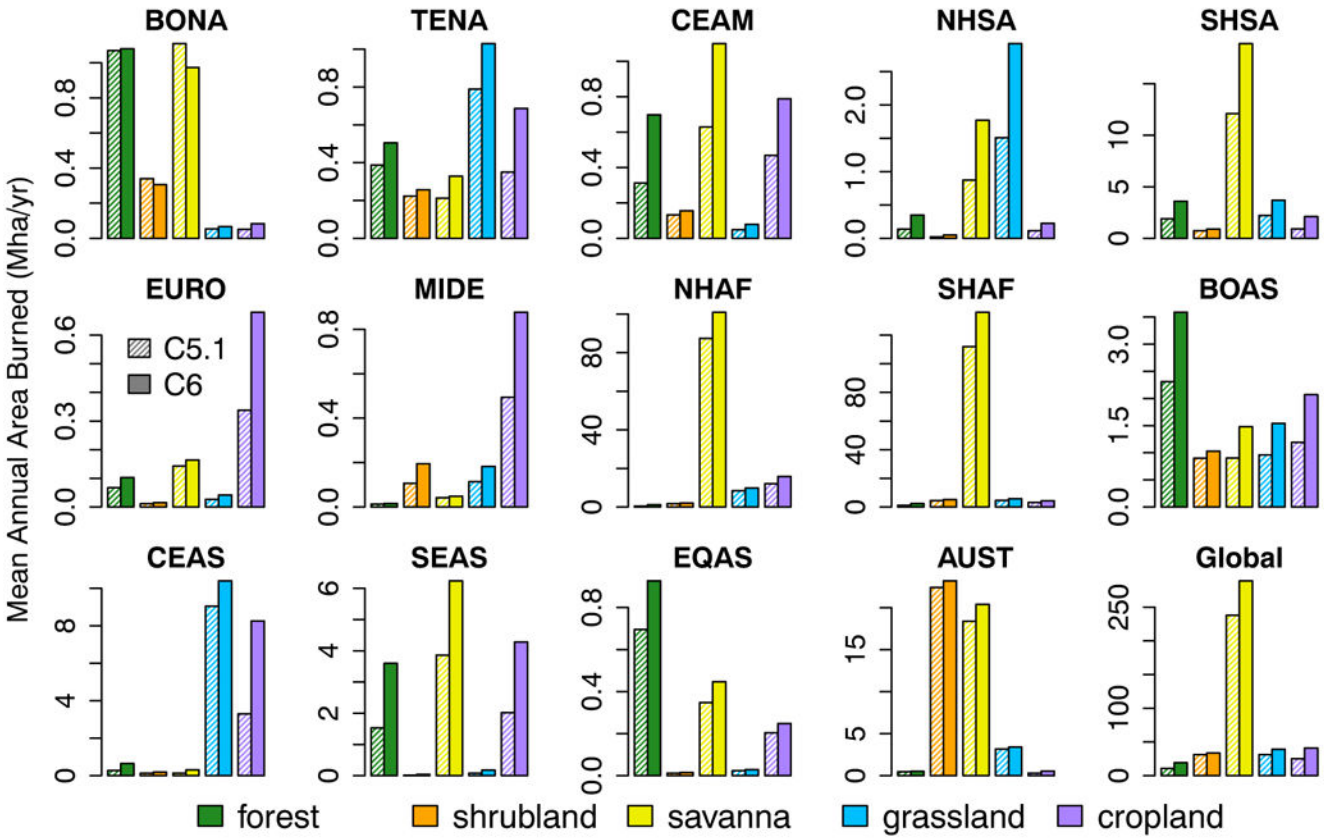

Fig. 6.

Regional 2002–2016 mean an-nual area burned for the C5.1 (hashed bars) and C6 (solid bars) MCD64A1 products, stratified by land cover class. The abbreviations used for the individual region names are listed in Table 3. Mean values take into account land cover changes as reported in the C5.1 MCD12Q1 land cover product for the years 2002–2013 only; for the years 2014–2016 the MCD64A1 burned area was partitioned using the 2013 MCD12Q1 product.

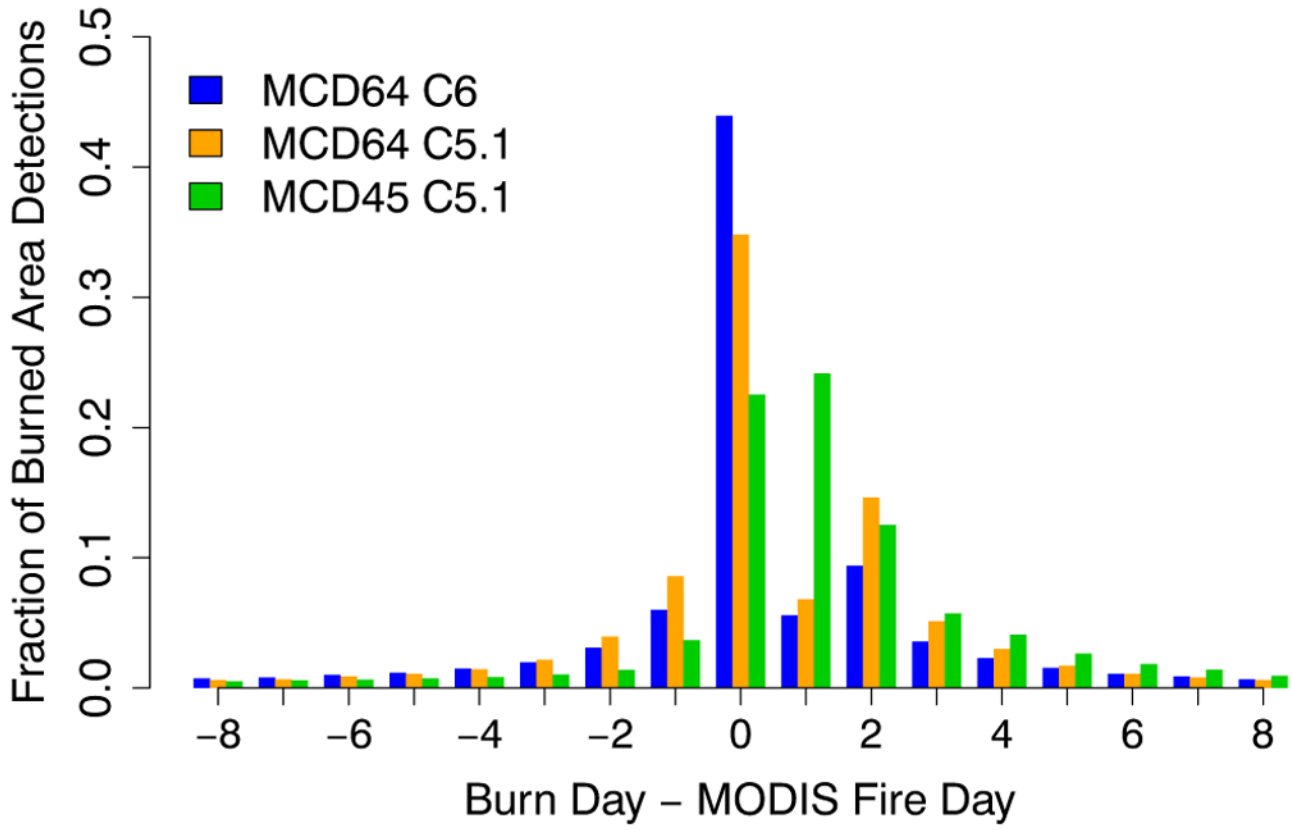

Fig. 7.

Histogram of time differences (in days) between spatially coincident MODIS MCD64 and MCD45 burned area and MODIS active fire detections for all MODIS land tiles during 2006. Negative numbers indicate that the MODIS active fire detection precedes the burned area detection.

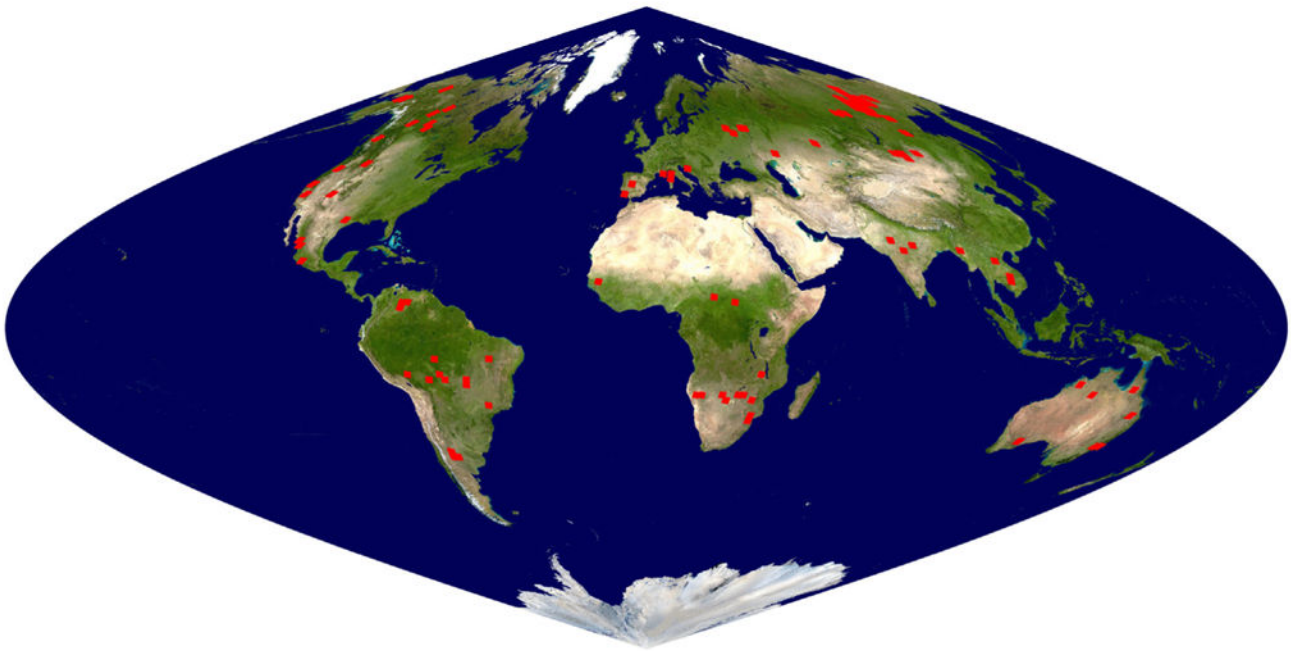

Fig. 8.

Location of the 108 Landsat 5 TM and Landsat 7 SLC-on ETM+ scenes used for validation. The location of the scenes was selected by trained interpreters, with the involvement of the GOFC GOLD regional networks, and all the reference data were generated via visual interpretation according to the CEOS Cal/Val Protocol. The Landsat acquisition dates range from 2000 to 2011.

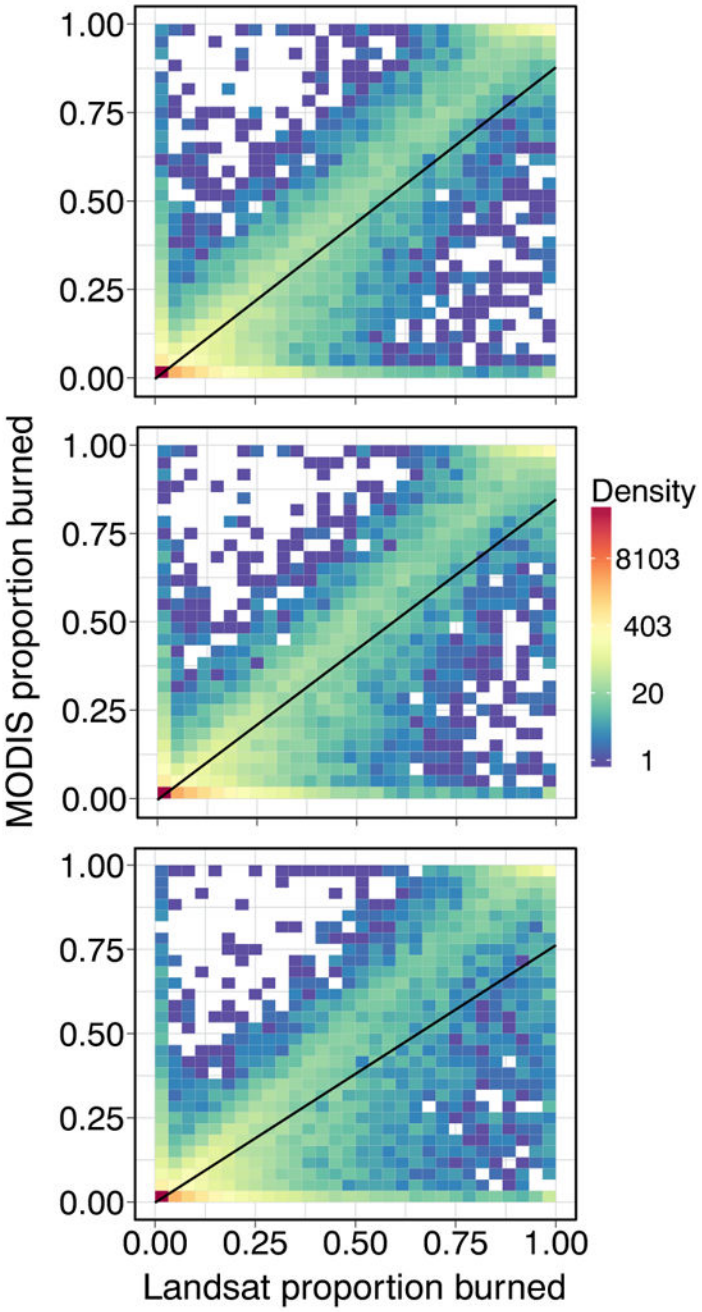

Fig. 9.

Scatter plots of the proportions of 5 km × 5 km cells labeled as burned by the MCD64A1 Collection 6 (*top*), MCD64A1 Collection 5.1 (*middle*), and MCD45A1 Collection 5.1 (*bottom*) products, plotted against the proportion labeled as burned by the reference dataset, considering all the independent reference data derived from 108 Landsat path/rows (Fig. 8). The point densities, calculated using a 50 × 50 quantization of the plot axes, are displayed with a rainbow logarithmic color scale. Regression results are as follows: C6 MCD64A1: 126,888 cells plotted, slope 0.88, intercept −0.003, r^2 = 0.818; C5.1 MCD64A1: 113,423

cells, slope 0.85, intercept −0.004, r^2 = 0.808; C5.1 MCD45A1: 122,991 cells, slope 0.76, intercept −0.002, r^2 = 0.744. (For interpretation of the references to color in this figure legend, the reader is referred to the web version of this article.)

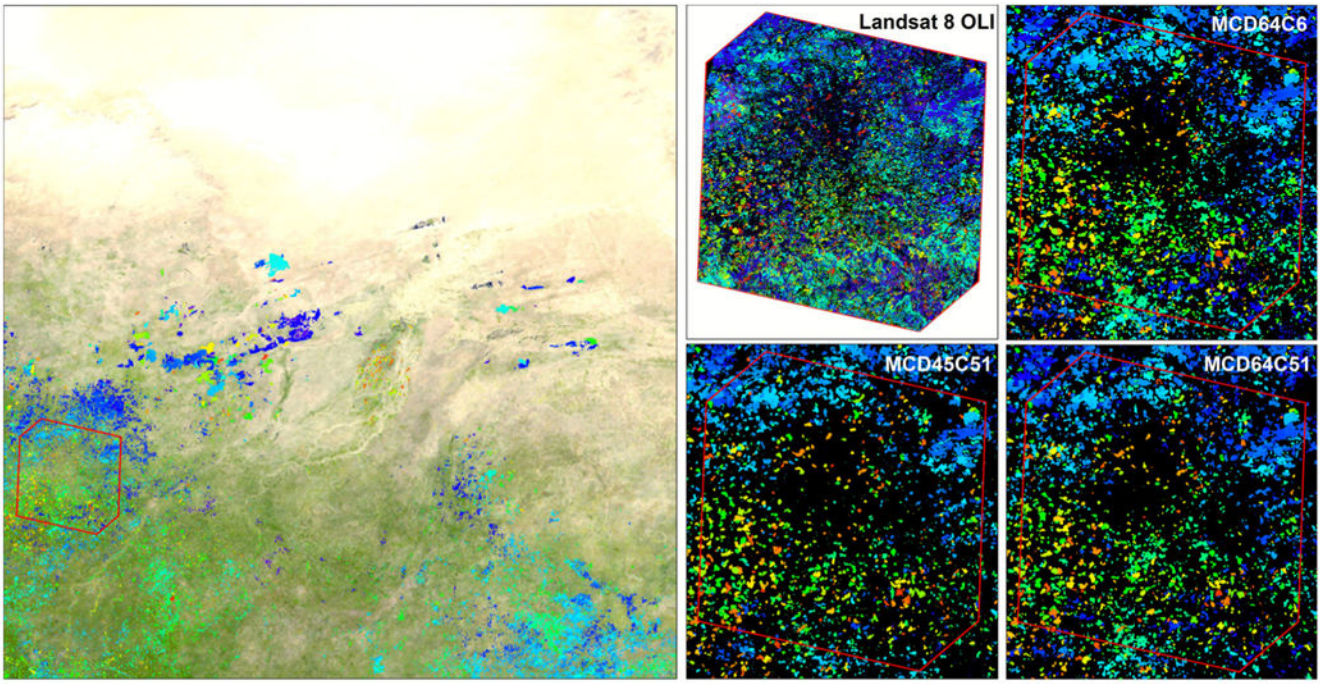

Fig. 10.

MODIS tile h17v07 (Mali) selected for consistency assessment of small burns. *Left*: burned areas detected by the Collection 6 MCD64A1 product from September 2013 to April 2014, represented with a rainbow scale indicating the day of burning, overlaid on MODIS Blue Marble true-color reflectance to provide geographic context. *Right*: cumulative map of the burned areas detected through the pair-wise interpretation of nine Landsat-8 OLI ~ 180 × 180 km images acquired between 28 September 2013 and 8 April 2014, and detail of the Collection 6 MCD64A1 (MCD64C6), Collection 5.1 MCD64A1 (MDC64C51), and Collection 5.1 MCD45A1 (MCD45C51) burned areas shown with the same scale and coverage as the Landsat reference data. (For interpretation of the references to color in this figure legend, the reader is referred to the web version of this article.)

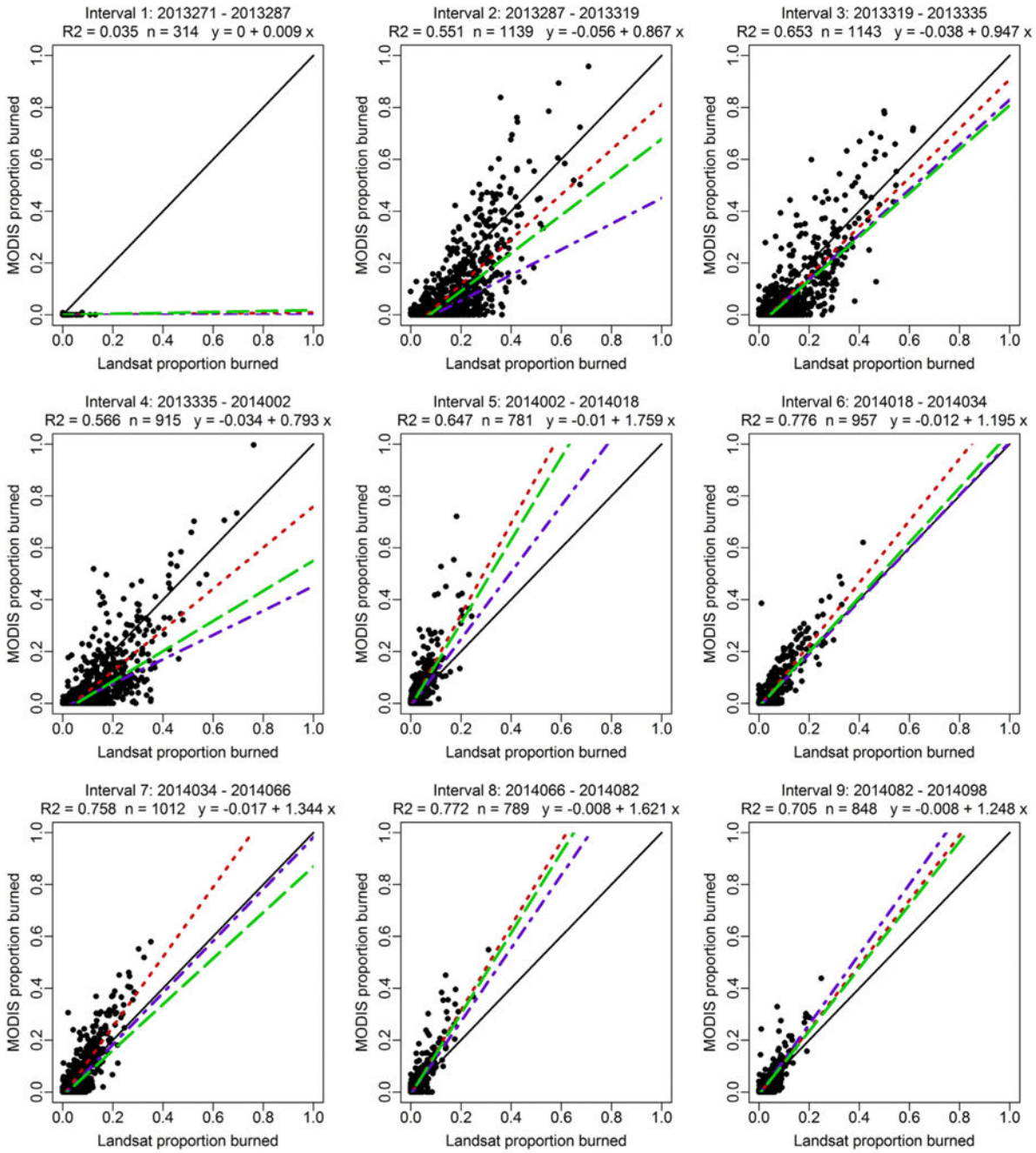

Fig. 11.

Regression of the proportion of area burned in coarse resolution cells between the MODIS burned area products and manually interpreted Landsat-8 OLI reference data for path WRS path/row 200/051 (Mali) in the 2013–2014 fire season. The individual data points (5 × 5 km cell values), regression coefficient, and regression line (red dotted line) are shown for the Collection 6 MCD64A1 product, whereas only the regression line is shown for the Collection 5.1 MCD64A1 (green dashed line) and Collection 5.1 MCD45A1 (purple dash-dot line) products. Only isolated burns at the beginning of the time series (time intervals 1

through 4) were not detected by the three products. (For interpretation of the references to color in this figure legend, the reader is referred to the web version of this article.)

Table 1

Spatial variables comprising the temporal change summary produced as part of the mapping algorithm.

Variable	Description
S^*	Maximum separability in VI time series
t^*	Date of maximum VI separability: $t^*(x, y) = (t_{k^*+W-1} + t_{k^*+W})/2$.
Δt^*	Uncertainty in date of maximum separability: $\Delta t^*(x, y) = t_{k^*+W-1} - t_{k^*+W}$.
ΔVI^*	Change in VI associated with maximum separability:
VI_{post}^*	Post maximum-separability VI
t_f	Cumulative mask identifying date on which active fire was detected during the three-month processing period.
IQR_{pre}^*	Interquartile range of observation dates in candidate pre-burn window associated with maximum separability
IQR_{post}^*	Interquartile range of observation dates in candidate post-burn window associated with maximum separability.
σ_t^*	Temporal “texture”, i.e., rank-filtered local standard deviation of t^*.

Table 2

Summary of major changes made to the Collection 5.1 MCD64A1 mapping algorithm for Collection 6.

Step/Section	Description of Change
Input data	Algorithm tuned for C6 MODIS surface reflectance and active fire products.
Time series extraction (3.1)	Adopted cloud minimum red-reflectance threshold to override MOD09 cloud mask.
Change summary (3.2)	Temporal window duration W reduced from 10 to 8 days.
Training samples (3.4)	Region growing no longer performed in cropland. New parameter coupling: $R_d = 2.5\sigma_p$.
Separability test (3.6)	Hellinger distance criterion eliminated; ΔVI* percentile criterion relaxed.
Prior probabilities (3.7)	P_{min} reduced to 0.01; σ_p default value reduced to 2 km.
Initial classification (3.9)	Posterior probability threshold reduced from 0.6 to 0.5.
Final classification (3.10)	Majority filter employs projection-aware kernel and is modulated using information derived from training data.

Table 3

Regional 2002–2016 mean annual area burned (Mha yr^{-1}), and relative change (Δ), for the MODIS Collection 5.1 and Collection 6 MCD64A1 burned area products. NH and SH denote the northern and southern hemispheres, respectively.

Region	Abbrv.	C5.1	C6	Δ (%)
Global	GLOB	336.5	422.5	26
Boreal North America	BONA	2.7	2.5	−6
Temperate North America	TENA	2.0	2.8	43
Central America	CEAM	1.6	2.8	77
NH South America	NHSA	2.7	5.3	100
SH South America	SHSA	17.8	29.3	64
Europe	EURO	0.6	1.0	71
Middle East	MIDE	0.8	1.4	80
NH Africa	NHAF	110.3	129.9	18
SH Africa	SHAF	125.3	153.7	23
Boreal Asia	BOAS	6.3	9.7	55
Central Asia	CEAS	12.9	19.9	54
Southeast Asia	SEAS	7.5	14.4	91
Equatorial Asia	EQAS	1.3	1.7	30
Australia and NZ	AUST	44.8	48.1	7

Table 4

Confusion matrix and accuracy metrics for the MCD64A1 Collection 6 and Collection 5.1 and MCD45A1 Collection 5.1 products, considering all the in-dependent reference data derived from 108 Landsat path/rows (Fig. 8). Accuracy metrics, which are described in the main text, consist of overall accuracy (OA), omission error (OE), commission error (CE), producer's accuracy (PA), user's accuracy (UA), and relative bias (B_{rel}).

MCD64 C6	Reference data				
	Burned	Unburned	*Row total*		
Burned [km^2]	76,520	23,808	100,327	OA	0.97
	(2.81%)	*(0.87%)*	*(3.67%)*	OE	0.37
Unburned [km^2]	45,705	2,581,562	2,627,268	CE	0.24
	(1.68%)	*(94.6%)*	*(96.3%)*	PA	0.63
Col. total [km^2]	122,225	2,605,370	2,727,595	UA	0.76
	(4.48%)	*(95.5%)*		B_{rel}	−17.9%
MCD64 C51	Reference data				
	Burned	Unburned	*Row total*		
Burned [km^2]	71,442	20,383	91,825	OA	0.97
	(3.08%)	*(0.88%)*	*(3.97%)*	OE	0.40
Unburned [km^2]	47,292	2,175,683	2,222,975	CE	0.22
	(2.04%)	*(94.0%)*	*(96.0%)*	PA	0.60
Col. total [km^2]	118,734	2,196,065	2,314,800	UA	0.78
	(5.13%)	*(94.9%)*		B_{rel}	–22.7%
MCD45 C51	Reference data				
	Burned	Unburned	*Row total*		
Burned [km^2]	63,926	19,406	83,332	OA	0.97
	(2.44%)	*(0.74%)*	*(3.18%)*	OE	0.45
Unburned [km^2]	51,710	2,483,134	2,534,845	CE	0.23
	(1.98%)	*(94.8%)*	*(96.8%)*	PA	0.55
Col. total [km^2]	115,636	2,502,541	2,618,176	UA	0.77
	(4.41%)	*(95.6%)*		B_{rel}	–27.9%